ARCHIVES
of
FOUNDRY ENGINEERING

ISSN (2299-2944)
Volume 2026
Issue 3/2026

153 – 173

10.24425/afe.2026.158030

19/3

Published quarterly as the organ of the Foundry Commission of the Polish Academy of Sciences

Cooling Rate and Gradient by Fe- and Mn-Rich Phases Precipitation in AlCuSi Alloys

P. Mikolajczak *
Poznan University of Technology, Poland
* Corresponding author. e-mail address: Piotr.Mikolajczak@put.poznan.pl

Received 23.07.2026; accepted in revised form 14.09.2026; available online 30.10.2026

Abstract

Gravity influences mold filling and solidification. In foundry engineering, apart from well-known gravity, centrifugal and pressure casting, technologies for casting by forced convection are being developed, where the application of a magnetic field plays a key role. Till now, the efficacy of forced flow in numerous studies have been conducted, including silicon extraction and aluminum alloys. The weakness of these studies is the fact, that they were conducted on small samples, mainly cylindrical shaped, where the cooling rate, gradient and temperature field were poorly investigated and discussed. In the present study, , thermal conditions like temperature gradient G and cooling rate R by the growth of occurring phases were studied using numerical simulation, concerning the facility applied in the investigations on the effect of rotating magnetic field. In cylindrical samples from base AlCuSi alloys, cooling rate R and temperature gradient G presented dependence from: calculation method for R and G (specified temperature or solid fraction in the T_L-T_S range), the place of measurement in the sample and from solid fraction curve determined by the alloy composition. β-$Al_9Fe_2Si_2$ phases precipitated at G=0.050-0.103 ˚C/mm and R=0.103-0.135 ˚C/s near to liquidus temperature and at G=0.043-0.387 ˚C/mm and R=0.318-0.404 ˚C/s near to solidus in AlCu4Si6Fe1 alloy, whilst at G=0.021-0.225 ˚C/mm and R=0.467-0.475 ˚C/s near to liquidus and at G=0.165-0.284 ˚C/mm and R=0.151-0.862 ˚C/s near to solidus in AlCu10Si10Fe1 alloy. $Al_{15}Si_2Mn_4$ phases precipitated at G=0.008-0.281 ˚C/mm and R=0.539-0.552 ˚C/s near to liquidus, whilst at G=0.050-0.322 ˚C/mm and R=0.292-0.356 ˚C/s near to solidus in the AlCu4Si6Mn2 alloy. In the prediction of secondary dendrite arm spacing and AlSi eutectic spacing new approach was tested and appropriate values of materials coefficient's have been established. Negligible impact of errors in processing parameters set by experimental procedure was observed.

Keywords: AlCuSi aluminum alloys, Solidification, Cooling rate, Temperature gradient, Fe- and Mn-rich phases, SDAS

1. Introduction

The unique combination of properties, like high strength-to-weight ratio, ductility, high corrosion resistance, non-toxicity, non-sparking, recyclability and weldability, makes aluminum alloys very attractive [1,2]. Aluminium casting alloys are popular in e.g. engine blocks and wheels production, while in plastic processing ductile aluminum alloys are applied as bridely used profiles, in aviation, marine and construction [3-8].

Cast aluminum alloys, as the major alloying elements contain Mg, Si and Cu [6-8]. Added to Al, copper (Cu) primarily causes increase in strength [9] and by higher content leads to increase in the hardness [10], whilst how the Cu element is distributed determines the strength and especially the ductility [11]. In aluminum-based AlCuSi alloys, the copper (Cu) lead to formation of ternary eutectic (α-Al + Al_2Cu + β-Si) and binary (α-Al + Al_2Cu). The impurities and sometimes intentional additions in Al alloys are zinc (Zn), manganese (Mn), and iron (Fe). The presence of iron causes formation of β-Al_5FeSi, whilst presence of manganese (Mn) leads to formation of $Al_{15}Si_2Mn_4$ phases. Therefore current study focusses on several alloys with compositions AlCu4Si6, that is close to popular in industry A319

© The Author(s) 2026. Open Access. This article is licensed under a Creative Commons Attribution 4.0 International License (http://creativecommons.org/licenses/by/4.0/), which permits use, sharing, adaptation, distribution and reproduction in any medium or format, as long as you give appropriate credit to the original author(s) and the source, provide a link to the Creative Commons licence, and indicate if changes were made.

and EN AC-45000 aluminum alloys, with composition: 3–5 wt.% Cu, 5–7 wt.% Si, 0.2–0.65 wt.% Mn and 1 wt.% Fe, and Al balanced.

During the solidification of alloys leading normally to dendritic structure, a number of processes take place simultaneously within the mushy: solute redistribution, crystallization, inter-dendritic fluid flow, ripening and solid movement. Metallic alloys may solidify with special rheological properties [12] resulting from a non-dendritic structure forming in the mushy zone in the presence of intensive melt stirring, finally leading to new production methods: electromagnetic processing of alloys [12-17], melt conditioning (HSMC or MC) [18,19], semisolid metal processing (SSM) [20], rheo- and thixo-casting [21-24]. In Direct Chill (DC) [8,25], melt stirring will be applied in order to dismiss defects like macro segregation and hot tearing [25-27] in billets.

The effect of forced convection generated by rotating magnetic field (RMF) was studied in directional solidification at front velocity v=0.04-0.12 mm/s and temperature gradient G=3 K/mm in iron and manganese containing AlSi alloys [28,29]. Similar to current study by slow bulk solidification, the microstructure in AlSiMg [30], AlCuSi [31], AlSiMn [32,33], AlSiFe [34] and AlSiMgFeMn [35] alloys was studied, supported by numerical simulation [36].

The production of photovoltaic cells, require mainly high-quality silicon produced by electromagnetic stirring EMS as the melt conditioning processing. Intensive investigations in this subject include are: separation of silicon from Al-Si [37-40] and Ti-Sn [41] melt, refining [42-44], separation [45] and morphology [46] of Si, and controlling segregation of impurities in silicon (Si) containing Al alloys [47-50].

In the scientific investigation mainly small simply shaped samples are applied, also on application of forced convection by production of the silicon [37-50] and aluminum [31-35] alloys. Located in the crucible and enveloped by coils and insulation, cylinder shaped samples were processed by stirring during solidification and microstructure of Al and Si alloys was studied.

Till now such studies [30-35,37-50] were focused on the microstructure, occurring in alloys phases, its amount and location, whilst the temperature evolution during solidification and stirring especially in the sample but also in the insulation envelope, in the cooling system and electromagnetic coils, were not discussed enough. Thermal parameters like solidification velocity, temperature gradient, cooling rate and temperature determine the growing microstructure in the castings and studied samples, whilst these aspects were poorly described or were completely omitted.

From the research on the silicon [39,40,43,47-50] and aluminum alloys [30-35], detailed data on thermal conditions were lacking, beside studies [48] where effect of rotating magnetic field on temperature homogenization was described.

In the current study on AlCuSi alloys with Fe and Mn addition (Table 1), main subject was the cooling rate R, temperature gradient G and temperature T in the sample (Fig. 1-2) by phases precipitation (Table 2). Additionally secondary dendrite arm spacing SDAS calculation as parameter characterizing microstructure was studied. Investigation was conducted in the facility (Fig. 1-2) [51] previously used to study the effect of forced flow on the Al alloys [30-36,39,40,43,47-50] by similar methodology. Thermal conditions were calculated using leading foundry software Magmasoft [52] and alloys were chosen according of specialized in thermodynamics Thermo-Calc [53] software.

Table 1.
The studied AlCuSi alloys.

Chemical composition [%]	T_L / T_S [˚C]	SDAS measured [µm]
AlCu4Si6Fe1	608.9 / 525.0	79.0
AlCu4Si6Mn0.65	610.9 / 524.1	100.0
AlCu4Si6Fe1Mn0.65	625.1 / 523.5	85.0
AlCu4Si6Fe2	638.2 / 523.8	-
AlCu4Si6Mn2	661.1 / 522.6	94.0
AlCu10Si10Fe1	610.0 / 521.5	66.0

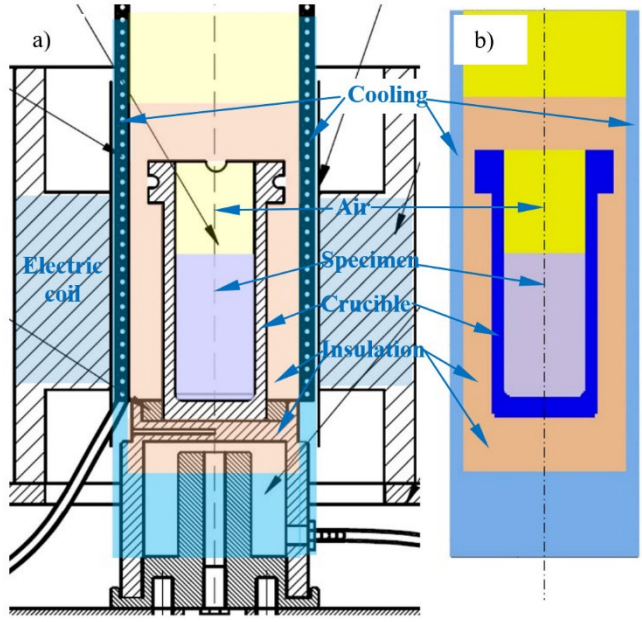


Fig. 1. The scheme of the applied facility: a) experimental facility, b) numerical model (mesh geometry)

2. Materials and methods

The settings for computer simulation leading to calculation of cooling rate, temperature gradient, temperature field, solidification time and others, together with experimental procedure applied, were below described.

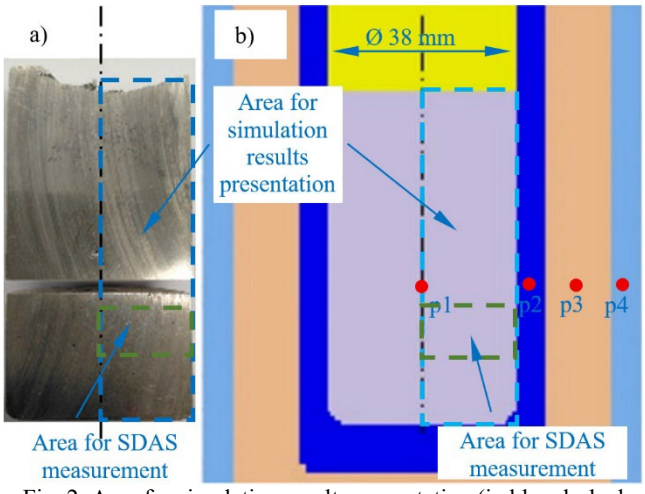


Fig. 2. Area for simulation results presentation (in blue dashed line rectangle): a) experimental specimen, b) numerical model (with thermocouples – red points). Green area selected for secondary dendrite arm spacing SDAS measurement

Table 2.
The studied AlCuSi alloys and occurring reaction during solidification

Chemical comp. [%]	Reaction	Temperature range of reaction [˚C]
AlCu4Si6Fe1	L → α-Al + L	608.9–601.1
	L → α-Al + β-$Al_9Fe_2Si_2$	601.1–560.4
	L → α-Al + β-$Al_9Fe_2Si_2$ + Si	560.4–525.0
AlCu4Si6Mn0.65	L → α-Al + L	610.9–593.6
	L → α-Al + $Al_{15}Si_2Mn_4$	593.6–561.5
	L → α-Al + $Al_{15}Si_2Mn_4$ + Si	561.5–524.1
AlCu4Si6Fe1Mn0.65	L → $Al_{15}Si_2Mn_4$ + L	625.1–608.8
	L → $Al_{15}Si_2Mn_4$ + L + α-Al	608.8–576.3
	L → $Al_{15}Si_2Mn_4$ + L + α-Al + β-$Al_9Fe_2Si_2$	576.3–559.6
	L → $Al_{15}Si_2Mn_4$ + α-Al + β-$Al_9Fe_2Si_2$ + Si	559.6–523.5
AlCu4Si6Fe2	L → β-Al_8Fe_2Si + L	638.2–608.0
	L → β-Al_8Fe_2Si + α-Al + L	608.0–603.5
	L → β-$Al_9Fe_2Si_2$ + L + α-Al	603.5–558.8
	L → β-$Al_9Fe_2Si_2$ + α-Al + Si	558.8–523.8
AlCu4Si6Mn2	L → $Al_{15}Si_2Mn_4$ + L	661.1–610.9
	L → $Al_{15}Si_2Mn_4$ + α-Al + L	610.9–560.2
	L → $Al_{15}Si_2Mn_4$ + α-Al + Si	560.2–522.6
AlCu10Si10Fe1	L → β-$Al_9Fe_2Si_2$ + L	610.0–559.6
	L → β-$Al_9Fe_2Si_2$ + α-Al + L	559.6–554.8
	L → β-$Al_9Fe_2Si_2$ + α-Al + L+ Si	554.8–521.6
	β-$Al_9Fe_2Si_2$ + α-Al + L+ Si → β-$Al_9Fe_2Si_2$ + α-Al + Si + Al_2Cu	521.6–521.5

The investigated AlCuSi alloys (Table 1) with Fe and Mn addition were prepared from high purity compounds according to the previously described methodology [30-35]. The alloy compositions (Table 1) were selected to achieve solidification in which the solid phase precipitates in a specific order and quantity (Fig. 3), including the phases precipitating in a specific order. Here, the different phases precipitate first, thus allowing for the appropriate planning of the reactions occurring in the alloys, which are presented in detail in Table 2.

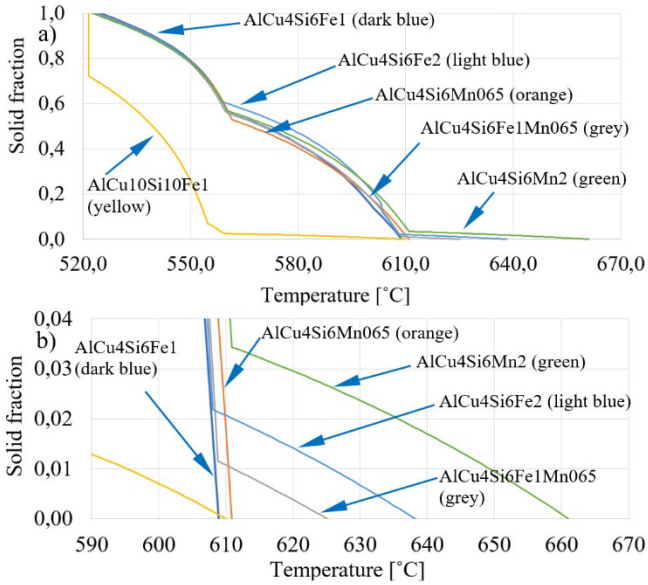


Fig. 3. Solid fraction fs curve in the studied alloys: a) fs in the range from 0.0 to 1.0 by temperature from 520 till 670 [˚C], b) fs from 0.0 to 0.04 by temperature from 590 till 670 [˚C]

Thermo-Calc software was applied for Property Diagrams calculation by equilibrium conditions and allowed to determine the phases precipitation sequence (Table 2).

In the AlCu4Si6Fe1 alloy (Table 2, Fig. 4a), the α-Al phase precipitated first according to the reaction L → α-Al + L in the temperature range of 608.9–601.1 ˚C, then the β-$Al_9Fe_2Si_2$ phase joins it and solidification takes place according to the reaction L → α-Al + β-$Al_9Fe_2Si_2$ in the range of 601.1–560.4 ˚C, then the AlSi-eutectics precipitate according to L → α-Al + β-$Al_9Fe_2Si_2$ + Si in the range of 560.4–525.0 ˚C and finally the solidification is completed at the solidus temperature of 525.0 ˚C.

In the AlCu4Si6Fe2 alloy (Table 2), the β-$Al_9Fe_2Si_2$ phase is precipitated first according to the reaction L → β-$Al_9Fe_2Si_2$ + L in the temperature range of 638.2–608.0 ˚C, then the α-Al phase joins it according to the reaction L → β-$Al_9Fe_2Si_2$ + α-Al + L in the temperature range of 608.0–558.8 ˚C, then the AlSi-eutectics precipitate according to L → β-$Al_9Fe_2Si_2$ + α-Al + Si in the temperature range of 558.8–523.8 ˚C and finally the solidification is completed at the solidus temperature of 523.8 ˚C.

In the AlCu4Si6Mn2 alloy, the composition was selected so that the $Al_{15}Si_2Mn_4$ phase was the first to precipitate (Table 2). Furthermore, the liquidus temperature T_L (Table 1) changed significantly, which resulted in the solid phase precipitating the earliest among the tested alloys (Fig. 3 a) and in a small amount (Fig. 3 b) as a result of the precipitation of the $Al_{15}Si_2Mn_4$ phase (Fig. 4 b).

In order to delay the precipitation of the solid phase, the AlCu10Si10Fe1 (Tab. 2) alloy was selected, in which the liquidus

temperature T_L is comparable to the AlCu4Si6Fe1 alloy and other used, i.e. 610.0 and 608.9 ˚C, respectively, however, the growth of the solid fraction proceeds initially in small amounts (Fig. 3a) due to the precipitation of β-$Al_9Fe_2Si_2$ (Fig. 4c), the solid fraction of which reaches only approx. 0.038.

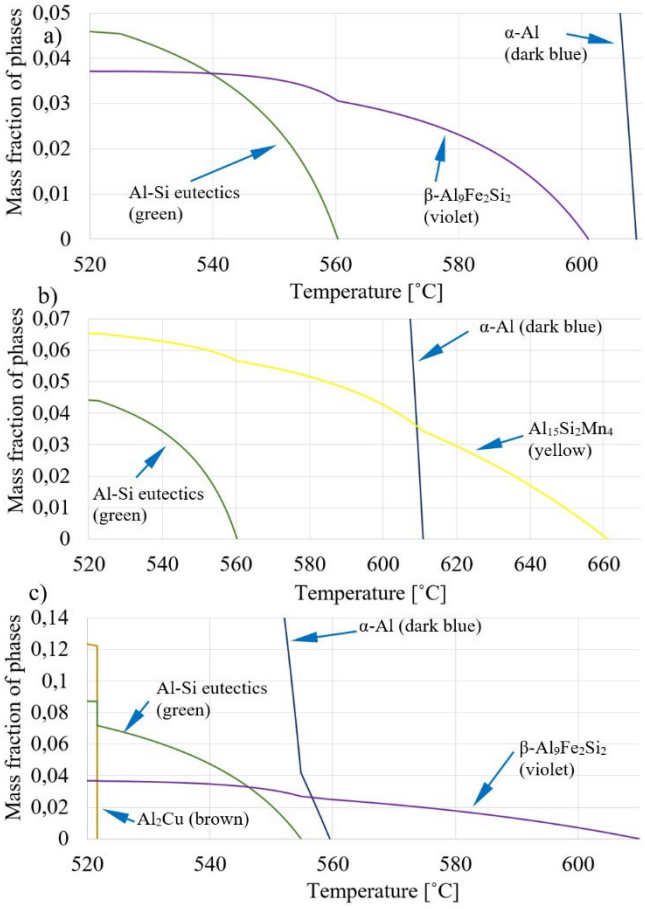


Fig. 4. Mass fraction of solid phases in the: a) AlCu4Si6Fe1, b) AlCu4Si6Mn2 and c) AlCu10Si10Fe1 alloys

Solidification experiments were conducted in a device (Fig. 1) [51] designed to study the effect of forced convection during slow volumetric solidification but with the magnetic field turned off. In the crucible, temperature measurements were conducted using a TP-203 thermocouple and an AR 207 (APAR, Poland) recorder. The melt crucible was separated from the coils (Fig. 1, 2b) by a copper water cooler (by flow rate 5-10 l/min) and an insulation layer (conductivity according to the manufacturer 0.1 W/mK, Fiberfrax). The sample (67 mm long and 19 mm in radius) were melted and held for 45 min at 800 ˚C (±3 ˚C), and then from a furnace transferred to the device (Fig. 1) within a crucible and finally solidified in it, at a low cooling rate of approximately 0.5-0.6 K/s and a temperature gradient of approximately 0.20-0.24 K/mm [32,33].

Similarly to previous [30-35], secondary dendrite arm spacing SDAS and eutectic spacing were measured as an average of approximately 15-45 dendrite branches in FIJI (ImageJ) software based on pictures from Nikon Eclipse MA200 and on samples (Fig. 2a) prepared using a standard metallographic procedure.

Solidification simulation without electromagnetic field and without filling in Magmasoft program [52] was conducted on the model concerning: the air, the cooling system, the crucible (dark blue), the sample (purple) and the insulation. In the virtual sample, crucible, insulation and cooling system, thermocouples were placed as presented in Fig. 2b (red points). The mesh was generated by Mode (Number of Elements) determining FV cubes with dimensions of about 1.0×1.0×1.0 mm and the whole geometry contained 301 401 cartesian cells. In simulation, alloys were prepared based on AlCu4Si6 alloy included in the standard Magmasoft database [52] and the chemical composition and solid fraction curve were modified. In applied in simulation AlCuSi alloys, the solid fraction curve with help of ThermoCalc software [53] was determined.

Thermophysical data for alloys based on Magmasoft's AlCu4Si6 were: density (Rho) 2144-2770 kg/m^3, specific heat (Cp) 870-1200 J/kgK, thermal conductivity (Lambda) 70-138 W/mK, whilst liquidus and solidus temperatures and solid fraction curve were additionally modified according to data (Tab. 1-2, Fig. 3) from ThermoCalc [53]. For modeling of cooling system material "Copper" and for crucible "Graphit" (graphite in German) from Magmasoft database were used. For Fiberfrax insulation, material "Insulation" was a base, by that thermophysical properties according to producer data were modified, and thermal conductivity by validation was determined. From the Magmasoft data base standard heat transfer coefficients (HTC constant) were also used: C7000 (7000 W/m^{2}K) and default.air (1500 W/m^{2}K).

Validation of the numerical simulation was performed based on a comparison of sample solidification times. Obtaining consistency in solidification times can be achieved by selecting thermophysical data or boundary conditions. In the analyzed casting-crucible-insulation-copper chill system, the Fiberfrax insulation has the lowest thermal conductivity and density, and its value significantly determines the heat transfer from the sample and crucible to the environment. Among the boundary conditions, the most significant change in sample solidification times could be achieved by selecting the HTC at the sample-crucible interface, because of its high conductivity, but both objects start to solidify at high 800 ˚C and have very similar temperature during experiment. To simplify validation, thermal conductivity of insulation was selected for consistency in solidification times, whilst boundary conditions were fixed at chosen high value 7000 W/m^{2}K (labeled C7000 in Magmasoft) allowing effective heat flow between objects. Of course for validation, balancing heat flow and finally temperature field in the studied, more thermal properties and boundary conditions might be modified, but by insulating properties of Fiberfrax, its low conductivity is the best choice. For simulations with specific alloys, Fiberfrax's thermal conductivity ("Lambda coefficient" in Magmasoft) was set to: 0.266 W/mK for the AlCu4Si6Fe1 alloy, 0.240 W/mK for the AlCu4Si6Mn0.65 alloy, 0.248 W/mK for the AlCu4Si6Fe1Mn0.65 alloy, 0.246 W/mK for AlCu4Si6Fe2, 0.234 W/mK for AlCu4Si6Mn2 and 0.2145 W/mK for the AlCu10Si10Fe1 alloy.

The main objective of this work was to evaluate the influence of the solid fraction curve on thermal conditions, i.e., cooling rate R, temperature gradient G, and temperature field T or liquid fraction FL during the precipitation of individual phases in alloys:

α-Al, β-$Al_9Fe_2Si_2$, $Al_{15}Si_2Mn_4$, and AlSi-eutectics. Another objective was to determine the secondary dendrite arm spacing (SDAS) by simulation and analyze the method of their calculation. The final objective was to assess the repeatability of experiments, the correctness of the experimental procedure and the proper desing of the device [51], . To assess the adequacy of the process parameters, the influence of the following process parameters was tested: thermal conductivity of the crucible, initial temperature of the cooling system, amount (mass) of the sample, liquidus temperature, alloy pouring temperature, initial temperature of the crucible, and initial temperature of the insulation around the crucible.

The author of the article used a well-known simulation software in the field of foundry engineering [52] and previously used thermophysical software [53]. The author carried out slow bulk solidification in a designed and manufactured device [51]. The perfectly determined alloys compositions, precisely prepared alloys from limited number and high purity components (e.g. 99.999% Al and 99.999% Cu from HMW-Hauner GmbH), predicted and limited occurring phases (β-$Al_9Fe_2Si_2$, $Al_{15}Si_2Mn_4$, α-Al, eutectics, Al_2Cu) which are well known by its morphology known from literature sources [54-56] and own research [30-35], all that ensured the reliability of the experimental microstructures obtained from solidified specimens.

3. Results and Discussion

The performed simulation and experimental studies included: a) solidification time, cooling rate and temperature gradient as well as general thermal conditions in the sample, crucible and device, b) evaluation and development of a method for calculating secondary dendrite arm spacing and Al-Si eutectic spacing, c) evaluation of experimental parameters influence on results.

3.1. Thermal conditions in the specimen and in the facility

For the assessment of the thermal conditions, will be analyzed: a) solidification time, temperature and liquid fraction, b) temperature gradient at each time step during solidification, c) temperature gradient and cooling rate calculated at the specified temperature or solid fraction.

3.1.1. Solidification time, temperature, and liquid fraction

3.1.1.1. Temperature

The numerical simulation (Fig. 5) provided results in the form of the temperature field of the copper chill, thermal insulation, crucible, and sample of the tested alloy at selected moments of the process, in 255 s (Fig. 5b) at 1.0% solidified specimen, in 428 s (Fig. 5c) at 50.0% solidified specimen, and in 627 s at 99.0% solidified specimen for the AlCu4Si6Fe1 alloy. The temperature difference between the sample and crucible (approximately 500-600 ˚C) and the insulation with chill (11-100 ˚C) is clearly visible. Fig. 5e shows a very even temperature field in the casting in the 5 s of the process, in the temperature range of 788-796 ˚C, where in the case of using a crucible with an initial temperature of e.g. 20 ˚C a significant temperature difference would be expected.

Temperature graphs (Fig. 6) at selected points (red points on Fig. 2a and Fig. 5a) confirmed the above observations from Fig. 5. The temperature in the copper chiller does not exceed 40 ˚C, and in the insulation 400 ˚C. The temperature in the crucible and the sample was similar during the entire process (Fig. 6b), and the temperature differences between points p1 (specimen alloy, Fig. 2a) and p2 (crucible graphite) reached values not greater than 3-6 ˚C. During the experiments, a thermocouple was placed in the crucible at a distance of approx. 3 mm from the cylindrical surface of the sample, while the sample itself had a diameter of 38 mm. A gradient of approx. 0.14 to 0.27 ˚C/mm was estimated and the value of 0.143 ˚C/mm from earlier experimental studies [51] concerning, among others, thermal conditions in the crucible and sample with detailed temperature measurements at selected points of the sample and in the crucible. Confirmation of the correctness of the design and slow cooling of the samples together with the crucible was obtained (Fig. 5 and 6) [51], which were then used to study the effect of forced convection on the microstructure of alloys [30-35].

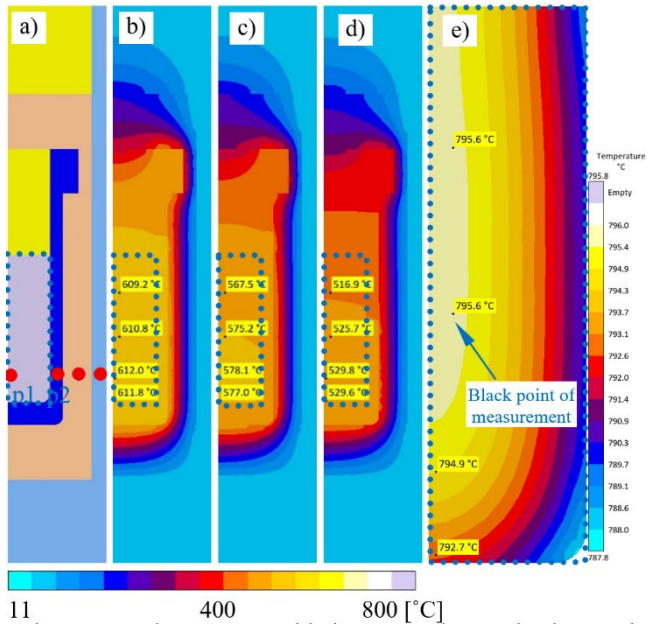


Fig. 5. a) Mesh geometry (with thermocouples – red points) and Temperature in the specimen and the facility (crucible, cooling, insulation) at the time: b) 255 s (1.0% solidified specimen), c) 428 s (50.0%) and d) 627 s (99.0%) for the AlCu4Si6Fe1 alloy, e) temperature in the specimen only at the time 5.0 s and temperature range 788.0-796.0 ˚C in the whole specimen. The blue dotted rectangle indicates the specimen on the figures a-d and also on figure e

The proper use of thermal insulation and water cooling was confirmed in Fig. 5 and 6. The electric coils for generating the rotating magnetic field (RMF) were effectively protected from the heat accumulated in the sample and crucible at an initial temperature of 800 ˚C. The coils were not damaged and can be reused repeatedly. The presence of high thermal conductivity objects in the system—an aluminum specimen, a graphite crucible,

and a copper chiller—as well as low thermal conductivity thermal insulation was used to correctly validate the thermal balance during the experimental process. In this situation, the most important factor determining the rate of heat flow is the thermal conductivity of the Fiberfrax insulation, and conductivity was modified to achieve compliance between experimental and simulation data.

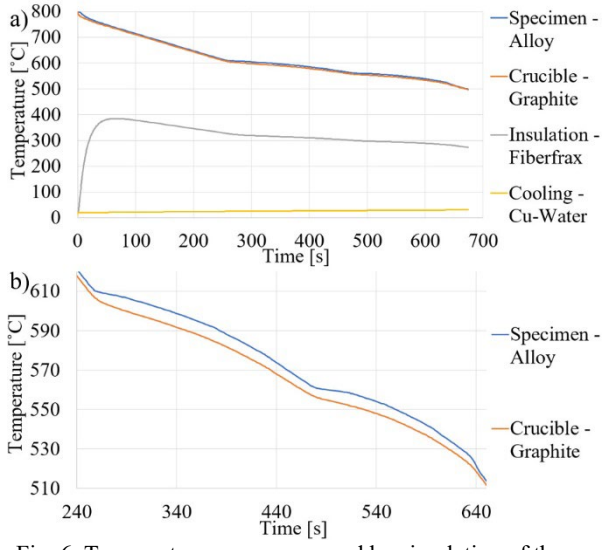


Fig. 6. Temperature curve measured by simulation of the AlCu4Si6Fe1 alloy, in the specimen center (alloy), in crucible, insulation and cooling, presented in the temperature range: a) from 800 to 0 ˚C, b) from 620 to 510 ˚C

Cooling curves (Fig. 7) measured in the center of the sample (red point p1, Fig. 2b), differ for the individual alloys. For the AlCu4Si6Fe1 and AlCu4Si6Mn2 alloys, they have a similar shape, but for the AlCu10Si10Fe1 alloy, the course is significantly different. These differences are related to the varied chemical compositions of the alloys (Table 1), the phases precipitated (Table 2, Fig. 4), and the resulting solid fraction curve (Fig. 3). In the AlCu4Si6Fe1 and AlCu4Si6Mn2 alloys, significant growth of the solid phase begins at a similar temperature of approximately 610 ˚C (Fig. 3b dark blue line and green line), and the solid fraction curve is also similar, therefore the cooling curves have a similar shape. It should be noted that the liquidus for AlCu4Si6Mn2 is 661.1 ˚C (Tab. 1, Fig. 3, green line), however, the first precipitated phase $Al_{15}Si_2Mn_4$ (Tab. 2, Fig. 4b, yellow line) constitutes a small fraction of the formed phases and therefore the increase in solid fraction is also small (Fig. 3b, green line), reaching only about 3.4% at a temperature of about 610 ˚C (mass fraction 0.034 on Fig. 4b, yellow line). Such a small portion of heat is not noticeable on the temperature curves (Fig. 7, orange line) in the range of 661.1-610 ˚C. In the AlCu10Si10Fe1 alloy, the liquidus temperature is 610.0 ˚C, but the first phase to precipitate is β-$Al_9Fe_2Si_2$ (Table 2), which precipitates in such an amount that at the initial temperature of α-Al phase precipitation it reaches only about 2.2% (mass fraction 0.022 on Fig. 4c, violet line). Such a small portion of the precipitated solid phase (Fig. 3a, yellow line) and heat portion is not noticeable on the temperature curves (Fig. 7, yellow line) in the range of 661.1-610 ˚C. Only from a temperature of about 560 ˚C, does significant precipitation of the solid phase occur (Fig. 3a, yellow line) due to the α-Al phase (Fig. 4c, dark blue line) and the temperature drop slows down (Fig. 7, yellow line). A large increase in the solid phase, from approximately 0.7 to 1.0 solid fraction (Fig. 3a, yellow line), occurs only near the solidus temperature, resulting in a visible horizontal plane in the alloy temperature course at 521.5 ˚C (Fig. 7, yellow line).

Solid fraction curves, varied by alloy composition, determine the cooling curves and the temperature field in the sample. They can influence the cooling conditions in the mushy zone and the crystallization conditions of individual precipitating phases, e.g., $Al_{15}Si_2Mn_4$, β-$Al_9Fe_2Si_2$, α-Al, and the entire microstructure. Therefore, they constitute the research objective of this work.

In the study of the AlSi30 alloy, Zou [48] carried out a numerical simulation in the Comsol software and these results showed convergence with the temperature course (Fig. 5e) in the currently tested sample. In the study [48], a sample (50 mm long and 40 mm in diameter) placed in a graphite crucible surrounded by an insulating material was subjected to solidification from an initial temperature of 850 ˚C. In the experiment under natural convection conditions, i.e. without the rotating magnetic field (RMF), immediately after the start of cooling (Fig. 2a in [48]) from the initial value of 850 ˚C, the temperature across the sample cross-section differed only by 6 ˚C, the minimum temperature was 838.0 ˚C and the maximum temperature was 844.0 ˚C. In the present study, after 5 s, i.e. just after the start of the cooling and solidification experiment, a temperature in the range of 790.9-795.6 was observed, e.g. at the half of the sample height, i.e. a difference of about 5 ˚C (Fig. 5e). Zou [48] also observed homogenization of the alloy and a reduction of the temperature range to 836.5–839 ˚C (2.5 ˚C) and 838.0–841.5 ˚C (3.5 ˚C), respectively, as a result of forced convection generated by an electromagnetic field of 15 mT and 5 mT.

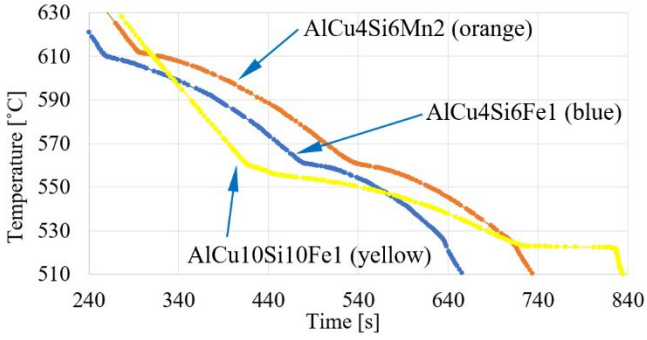


Fig. 7. Temperature curves measured by simulation, in the specimen center (alloy), in alloys with strongly differentiating solid fraction curves (seen on Fig. 3 and 4)

The effect of an alternating electromagnetic field on the separation of pure silicon was investigated experimentally and by simulation in the AlSi45 alloy. The temperature field (in Fig. 7b in [45]) during solidification carried out in a graphite crucible with an internal radius of 14 mm using thermal insulation showed a horizontal course of temperature isotherms. In the present results, 3–5 ˚C was observed (Fig. 5 b–e and Fig. 6 b), which is consistent with the results of Xue [45] where the temperature difference between the edge of the crucible and the center of the sample is about 0–5 ˚C.

Jiang [46] subjected AlSi alloys (with silicon content ranging from 35 to 65%) to directional solidification in an electromagnetic field in a high-purity graphite crucible with a height of 90 mm and an internal radius of 10 mm. Numerical simulations [46] showed almost uniform horizontal temperature isolines and suggested a uniform temperature distribution in the cross-section of the crucible and the sample, with an obvious preservation of the temperature gradient in the conducted directional solidification, where a temperature difference of about 40 ˚C was observed between the lower and upper parts of the sample.

In a high-purity and high-density graphite crucible with an internal radius of 8.5 mm and a length of 65 mm, Lv [37] investigated the separation of silicon in an AlSi45 alloy during directional solidification under conditions of electromagnetically forced convection. In a numerical simulation, Lv [37] showed almost horizontal temperature isolines, similar temperatures in the sample and crucible, while maintaining the conditions of directional solidification, i.e. a difference of about 200 ˚C (Fig. 6a in [37]) in the temperature distribution between the lower and upper parts of the crucible.

3.1.1.2. Fraction liquid

Instead of the temperature field, it is more convenient to analyze the liquid phase or the solid phase to observe the solidification progress, e.g., in Magmasoft marked as Fraction Liquid FL [%] or Fraction Solid FS [%]. The Fraction Liquid FL [%] (Fig. 8) shows that the mushy zone moves predominantly from the upper part of the sample to the lower part, and in the lower part at a later stage of solidification (Fig. 8 b-d); the solidification direction also leads from the crucible wall to the cylindrical axis of the sample. It is clear that the mushy zone is extensive; it is impossible to find an area with FL values of 0% and FL 100% in the simulation results at one moment in the process.

3.1.1.3. Solidification time

The solidification time of the AlCu4Si6Fe1 alloy is 638.3 s in the lower part of the sample and 604.9 s in the upper part (Fig. 9a). The solidification time isolines in Fig. 9a-e run almost horizontally. The samples can be considered to solidify almost simultaneously in the entire space, because also in the horizontal section the differences in solidification time do not exceed about 4 s, with a total solidification time of, e.g., 638.3 s for the AlCu4Si6Fe1 alloy. The upper part of the sample solidifies slightly faster, and the lower part solidifies as last, so there is a weak tendency of front moving towards the lower part, visible for all alloys (Fig. 9). The results of Fraction Liquid FL (Fig. 8) were confirmed by Solidification time ST (Fig. 9a), where the AlCu4Si6Fe1 sample was almost completely solidified for the time step of 573 s (Fig. 8d, the solid fraction was 90% in the whole sample), and the solidification time was 638.3 s (Fig. 9a). Microstructural parameters may slightly differ in the lower and upper parts and in the middle and outer parts of the sample as a result of the small variation in solidification time. In [45], attention was paid to the more intense cooling of the upper part of the sample as a result of the heat flow from the sample upwards through the crucible, which is consistent with the present results (Fig. 8 and 9). Based on the evolution stages of the liquid phase field (Fig. 8 a-d), solidification times (Fig. 9 a-f) and temperature field (Fig. 5b-e), it can be concluded that solidification occurs slowly and evenly, almost at the same time in the entire sample volume, which in the AlCu4Si6Fe1 alloy leads to a uniform distribution of the dendritic structure [31]. The microstructure evaluation zone in the tested AlCuSi alloy samples was located in the area of the last solidification (Fig. 9), i.e. in the lower part (Fig. 2 a-b, green rectangle area).

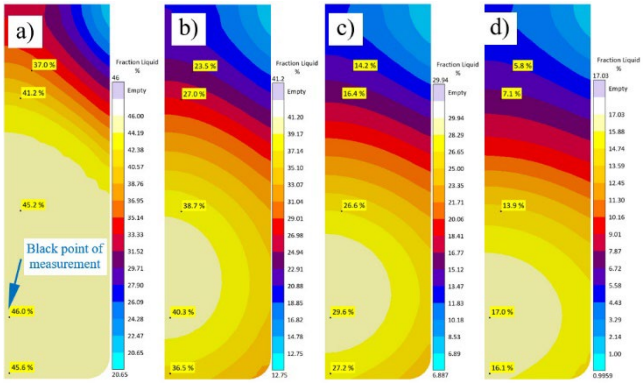


Fig. 8. Fraction liquid FL [%] in the AlCu4Si6Fe1 alloy specimen at the time (and percent of the whole specimen solidified): a) t=469 s, 60%, b) t=502 s, 70%, c) t=534 s, 80%, d) t=573 s, 90%

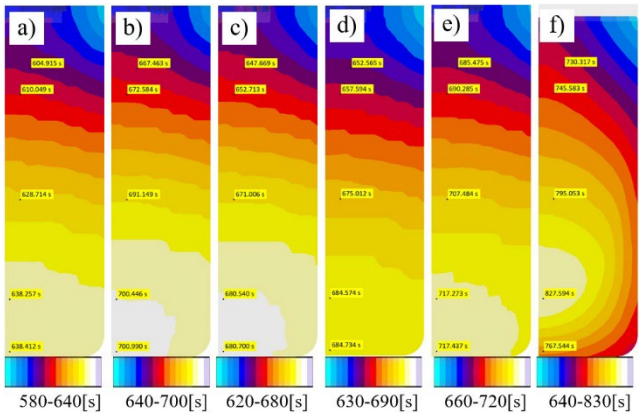


Fig. 9. Solidification time ST [s] in the specimen made of: a) AlCu4Si6Fe1, b) AlCu4Si6Mn0.65, c) AlCu4Si6Fe1Mn0.65, d) AlCu4Si6Fe2, e) AlCu4Si6Mn2, f) AlCu10Si10Fe1

3.1.2. Gradient time GT

In addition to Temperature, Fraction Liquid, and Solidification time, thermal conditions in the casting can be assessed, for example, based on temperature gradient, cooling rate, and velocity, as well as other parameters, such as those built on the Niyama criterion. Magmasoft features the Gradient time GT [˚C/mm] parameter, which provides the temperature gradient across the entire casting at a selected time. Fig. 10a shows the gradient time corresponding to the Fraction liquid FL field (Fig. 8a) at 469 s, i.e., when 60% of the entire sample has solidified. As the process time progresses from 469 to 573 s and the sample solidifies significantly, the gradient value changes: higher values initially observed at the top (Fig. 10a) gradually shift toward the bottom of the sample (Fig. 10c-d). Based on the comparison of Fraction liquid FL (Fig. 8d) and gradient time GT [˚C/mm] (Fig. 108), it can be concluded that higher gradient values occur in the area where there

is a high degree of solidification (low Fraction Liquid value) or even the solidus temperature has been reached. For example, in Fig. 10d, at half the sample height, the gradient time GT increased to 0.270 [˚C/mm] from the initial value of 0.144 [˚C/mm] (Fig. 10a), and in the same place Fraction liquid dropped to 13.9% (Fig. 8d). In experimental studies [31], the temperature gradient measured and calculated between the specimen center and a location 4 mm away from the specimen's surface achieved for solidification without stirring $G_{800\text{-}liq}$ = 0.196 (K/mm) and $G_{liq\text{-}470}$ = 0.132 (K/mm). These data were confirmed by the values of 0.144, 0.109, 0.218 and 0.270 ˚C/mm at half the sample height in Fig. 10 a-d. This confirmed the correctness of the design for conducting slow solidification and studying the effect of convection on the microstructure, and indicated the correctness the validation by modifying the thermal properties (conductivity) of the insulation Fiberfrax only.

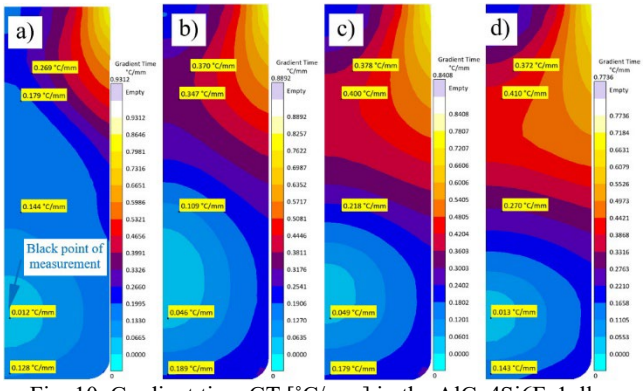


Fig. 10. Gradient time GT [˚C/mm] in the AlCu4Si6Fe1alloy specimen at the time (and percent of the whole specimen solidified): a) t=469 s, 60%, b) t=502 s, 70%, c) t=534 s, 80%, d) t=573 s, 90%

3.1.3. Cooling rate R and Gradient G

For the assessment of the thermal conditions, temperature gradient and cooling rate will be calculated and analyzed at the specified temperatures: liquidus temperature T_L (solid fraction f_s=0.0%), solidus temperature T_S (solid fraction f_s=100%) and at temperatures corresponding to various solid fraction values (f_s=2, 25, 75 and 98%).

The casting microstructure is essentially determined by the T_L-T_S solidification range, and that's is why this range is of most interest to the foundryman. Therefore, it is worthwhile to analyze parameters characterizing the thermal conditions within the casting's solidification range, in the mushy zone. Unlike the Temperature field, Liquid Fraction, or Gradient time, the parameter Gradient G [˚C/mm] provides the temperature gradient values at a selected location when the isoline of a specific temperature (or solid phase fraction) is reached in a selected mesh element in the finite volume (FV). To characterize the solidification range in this way, temperature isolines within the solidification range must be selected. In Magmasoft, this temperature is called the Thermo Criteria Temperature (TCT) ˚C and is set by default in the alloy database to a temperature higher than or equal to the liquidus temperature. For example, in the Magmasoft database for the AlSi6Cu4 alloy, the TCT is by default 612.00 ˚C by the liquidus temperature of T_L=610.00 ˚C.

3.1.3.1. Gradient G for T_L and f_s = 0.00%

In the tested alloys, the Gradient G (Fig. 11) calculated for the liquidus temperature T_L (constant fraction f_s = 0.00%) reached values in the range of approximately 0.009–0.74 ˚C/mm.

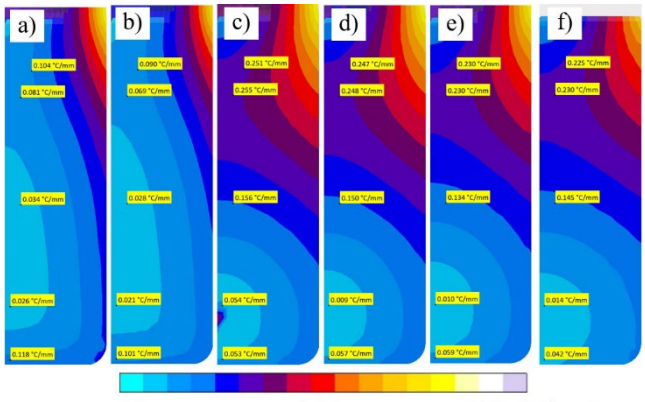


Fig. 11. Gradient G [˚C/mm] calculated by T_L (f_s=0.00%) in the specimen made of: a) AlCu4Si6Fe1, b) AlCu4Si6Mn0.65, c) AlCu4Si6Fe1Mn0.65, d) AlCu4Si6Fe2, e) AlCu4Si6Mn2, f) AlCu10Si10Fe1

At half the sample height, the Gradient G reached values of 0.034 and 0.028 ˚C/mm in the AlCu4Si6Fe1 and AlCu4Si6Mn0.65 alloys, while 0.156, 0.150, 0.134 and 0.145 ˚C/mm in the AlCu4Si6Fe1Mn0.65, AlCu4Si6Fe2, AlCu4Si6Mn2 and AlCu10Si10Fe1 alloys, respectively. In the upper part of the sample, Gradient G reached values of 0.104 and 0.090 ˚C/mm in the AlCu4Si6Fe1 and AlCu4Si6Mn0.65 alloys, while 0.251, 0.247, 0.230 and 0.225 ˚C/mm in the AlCu4Si6Fe1Mn0.65, AlCu4Si6Fe2, AlCu4Si6Mn2 and AlCu10Si10Fe1 alloys, respectively. In the lower part of the sample, Gradient G reached values of 0.026, 0.021, 0.054, 0.009, 0.010 and 0,014 ˚C/mm in the AlCu4Si6Fe1, AlCu4Si6Mn0.65, AlCu4Si6Fe1Mn0.65 AlCu4Si6Fe2, AlCu4Si6Mn2 and AlCu10Si10Fe1 alloys respectively. The studied alloys can be clearly divided into two groups in this respect, and this division is consistent with the solid phase fraction curve. In the first group (AlCu4Si6Fe1 and AlCu4Si6Mn0.65) a significant precipitation of the solid phase occurs already from the liquidus, while in the second group (AlCu4Si6Fe1Mn0.65, AlCu4Si6Fe2, AlCu4Si6Mn2 and AlCu10Si10Fe1 alloys) after reaching the liquidus, small amounts of the solid phase are initially precipitated. It can be concluded that the first α-Al phases precipitated just at the liquidus (Fig. 4, Table 2) in the AlCu4Si6Fe1 and AlCu4Si6Mn0.65 alloys grew at a lower temperature gradient (0.034 and 0.028 ˚C/mm) than the β-$Al_9Fe_2Si_2$ and $Al_{15}Si_2Mn_4$ phases (Fig. 4, Table 2) in the AlCu4Si6Fe1Mn0.65, AlCu4Si6Fe2, AlCu4Si6Mn2 and AlCu10Si10Fe1 alloys, where the gradient was approximately 0.156, 0.150, 0.134 and 0.145 ˚C/mm, respectively. In general, it can be stated that in all tested alloy samples, the G values in the upper and outer part of the sample are higher than in the lower and inner part. In the studies on the influence of the magnetic field [30-35], the analysis of microstructure parameters was carried out for the lower part of the sample (measurement location in the green

rectangle in Fig. 2). In each tested alloy, the G gradient differs in the cross-section from the edge of the sample to the center, which means that the solid phases growing at the edge of the sample had different cooling rates than those in the center, e.g. in the AlCu4Si6Fe1 alloy (Fig. 11a), the α-Al phase grew (Fig. 4a, α-Al dark blue) with a gradient from 0.026 ˚C/mm (Fig. 11a) to about 0.165 ˚C/mm.

3.1.3.2. Gradient G for T_S and f_s = 100.00%

In the tested alloys, the gradient G (Fig. 12) calculated for the solidus temperature T_S (solid fraction f_s = 100.00%) reached values in the range of approximately 0.049–0.76 ˚C/mm.

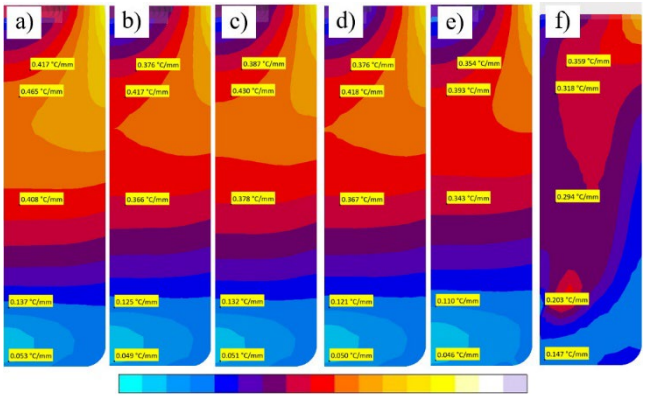


Fig. 12. Gradient G [˚C/mm] calculated by T_S (f_s =100.0%) in the specimen made of: a) AlCu4Si6Fe1, b) AlCu4Si6Mn0.65, c) AlCu4Si6Fe1Mn0.65, d) AlCu4Si6Fe2, e) AlCu4Si6Mn2, f) AlCu10Si10Fe1

At half the sample height, the gradient G reached values of 0.408, 0.366, 0.378, 0.367 and 0.343 ˚C/mm in the AlCu4Si6Fe1, AlCu4Si6Mn0.65, AlCu4Si6Fe1Mn0.65, AlCu4Si6Fe2 and AlCu4Si6Mn2 alloys, respectively, while 0.294 ˚C/mm in the AlCu10Si10Fe1 alloy. In the upper part of the sample, Gradient G reached values of 0.417, 0.376, 0.387, 0.376 and 0.354 ˚C/mm in the AlCu4Si6Fe1, AlCu4Si6Mn0.65, AlCu4Si6Fe1Mn0.65, AlCu4Si6Fe2 and AlCu4Si6Mn2 alloys, respectively, while 0.359 ˚C/mm in the AlCu10Si10Fe1 alloy. In the lower part of the sample, Gradient G reached values of 0.137, 0.125, 0.132, 0.121 and 0.110 ˚C/mm in the AlCu4Si6Fe1, AlCu4Si6Mn0.65, AlCu4Si6Fe1Mn0.65, AlCu4Si6Fe2 and AlCu4Si6Mn2 alloys, respectively, while 0.203 ˚C/mm in the AlCu10Si10Fe1 alloy. Due to the values and distribution of the gradient on the sample cross-section, clear differences can be seen for the AlCu10Si10Fe1 alloy. The phases precipitating in the lower part of the sample (measurement area, Fig. 1 and 2) precipitate around the solidus temperature in the AlCu4Si6Fe1, AlCu4Si6Mn0.65, AlCu4Si6Fe1Mn0.65, AlCu4Si6Fe2, and AlCu4Si6Mn2 alloys at a lower gradient than in the case of the AlCu10Si10Fe1 alloy. This differentiation is related to the solid phase curve (Fig. 3a), where it is clearly visible that in the solidus area of the AlCu10Si10Fe1 alloy, a significant increase in the solid phase occurs and, consequently, the release of latent heat of solidification occurs. Generally speaking, it can be stated that in all tested alloy samples, the G values in the upper part and the sample are higher than in the lower part. In the studies of the influence of the magnetic field [30-35], the analysis of microstructure parameters was carried out for the lower part of the sample, where the values in the cross-section from the center to the outer part are very uniform, i.e. the phases precipitated in the sample axis and at the edge had identical solidification conditions (measurement location in the brown rectangle in Fig. 2). In the AlCu10Si10Fe1 alloy, this distribution is slightly more complex and uneven.

3.1.3.3. Cooling rate R for T_L and f_s = 0.00%

Another important parameter characterizing the solidification zone, similarly to the temperature gradient [˚C/mm] and the front velocity [mm/s], is the cooling rate [˚C/s], calculated similarly to the gradient G based on a specific temperature (Thermo Criteria Temperature TCT ˚C), when a specific TCT isoline passes through a selected point of the sample (the mentioned FV grid cell). The cooling rate R (Fig. 13) (f_s=0.00%) reached values in the range of approximately 0.082–0.64 ˚C/mm. The cooling rate R (Fig. 13), calculated for the liquidus temperature T_L (f_s=0.0%), reached at half the sample height the values of 0.097 (Fig. 13a) and 0.082 ˚C/s (Fig. 13b) in the AlCu4Si6Fe1 and AlCu4Si6Mn0.65 alloys, respectively, while 0.520, 0.515, 0.495 and 0.449 ˚C/s (Fig. 13b-f) in the AlCu4Si6Fe1Mn0.65, AlCu4Si6Fe2, AlCu4Si6Mn2 and AlCu10Si10Fe1 alloys, respectively.

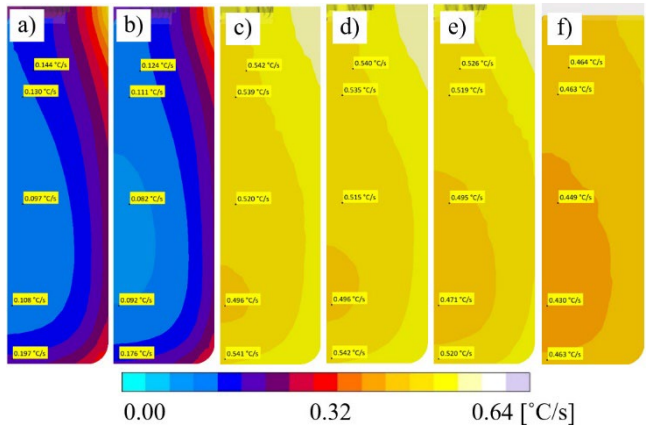


Fig. 13. Cooling rate R [˚C/s] calculated by T_L (f_s =0.0%) in the specimen made of: a) AlCu4Si6Fe1, b) AlCu4Si6Mn0.65, c) AlCu4Si6Fe1Mn0.65, d) AlCu4Si6Fe2, e) AlCu4Si6Mn2, f) AlCu10Si10Fe1

In the upper part of the sample, the cooling rate R reached the values of 0.144 (Fig. 13a) and 0.124 ˚C/s (Fig. 13b) in the AlCu4Si6Fe1 and AlCu4Si6Mn0.65 alloys, respectively, while 0.542, 0.540, 0.526 and 0.464 ˚C/s (Fig. 13b-f) in the AlCu4Si6Fe1Mn0.65, AlCu4Si6Fe2, AlCu4Si6Mn2 and AlCu10Si10Fe1 alloys, respectively. The alloys can be clearly divided into two groups in this respect, and this division is consistent with the solid phase fraction curve. In the first group (AlCu4Si6Fe1 and AlCu4Si6Mn0.65), significant solid phase precipitation occurs from the liquidus stage, whereas in the second group (AlCu4Si6Fe1Mn0.65, AlCu4Si6Fe2, AlCu4Si6Mn2, and AlCu10Si10Fe1), after reaching the liquidus stage, small amounts of solid phase are initially precipitated, allowing for a higher cooling rate. In the first group, there is also greater variation in

values across the cross-section, from the cylindrical axis of the sample to its outer part.

3.1.3.4. Cooling rate R for T_S and f_s = 100.00%

The cooling rate R (Fig. 14) calculated for half the sample height at the end of the solidification front (f_s=100%) reached values in the range of approximately 0.021–0.67 ˚C/s. The cooling rate R (Fig. 14), calculated for the solidus temperature T_S (f_s=100.0%), reached at half the sample height the values of 0.567, 0.511, 0.535, 0.530 and 0.501 ˚C/s in the AlCu4Si6Fe1, AlCu4Si6Mn0.65, AlCu4Si6Fe1Mn0.65, AlCu4Si6Fe2 and AlCu4Si6Mn2 alloys, respectively, while 0.180 ˚C/s (Fig. 14f) in the AlCu10Si10Fe1 alloy. In the upper part of the sample, the cooling rate R reached values of 0.428, 0.396, 0.416, 0.414 and 0.393 ˚C/s in the AlCu4Si6Fe1, AlCu4Si6Mn0.65, AlCu4Si6Fe1Mn0.65, AlCu4Si6Fe2 and AlCu4Si6Mn2 alloys, respectively, while 0.150 ˚C/s in the AlCu10Si10Fe1 alloy. Due to the values and distribution of the gradient on the sample cross-section, clear differences can be seen for the AlCu10Si10Fe1 alloy. The phases precipitating in the upper and middle parts of the sample precipitate around the solidus temperature in the AlCu4Si6Fe1, AlCu4Si6Mn0.65, AlCu4Si6Fe1Mn0.65, AlCu4Si6Fe2 and AlCu4Si6Mn2 alloys at a higher cooling rate (ca. 0.520 ˚C/s) than in the case of the AlCu10Si10Fe1 alloy (ca. 0.180 ˚C/s). However, in the lower part of the sample (area of measurement, Fig. 1 and 2) in the AlCu10Si10Fe1 alloy, a strong increase and differentiation of the cooling rate in the cylindrical axis of the sample and in its external part occurred, where R takes values from 0.15 to 1.129 ˚C/s. This differentiation is related to the solid phase curve (Fig. 3), where it is clearly visible that in the solidus region of the AlCu10Si10Fe1 alloy, a significant increase in the solid phase occurs, resulting in the release of latent heat of solidification. Generally speaking, it can be concluded that in all tested alloy samples, the R values in the upper part of the sample are lower than in the lower part, and the highest values are found in the measurement zone (Fig. 1,2). In studies of the effect of the magnetic field [30-35], the analysis of microstructure parameters was carried out for the lower part of the sample, and there, in the cross-section from the cylindrical axis of the sample to the outer part, the values are different, i.e., the phases precipitated in the sample axis and at the edge had different solidification conditions (measurement area in the green rectangle in Fig. 2). In the AlCu10Si10Fe1 alloy, this distribution is more complex and most diverse. In each tested alloy, the cooling rate R varies across the cross-section from the edge of the sample to the center, which means that the solid phases growing at the edge of the sample had different cooling rates than those in the center, e.g., the α-Al phase grew at a rate R from 0.663 ˚C/s to about 0.530 ˚C/s in the AlCu4Si6Fe1 alloy (Fig. 14a).

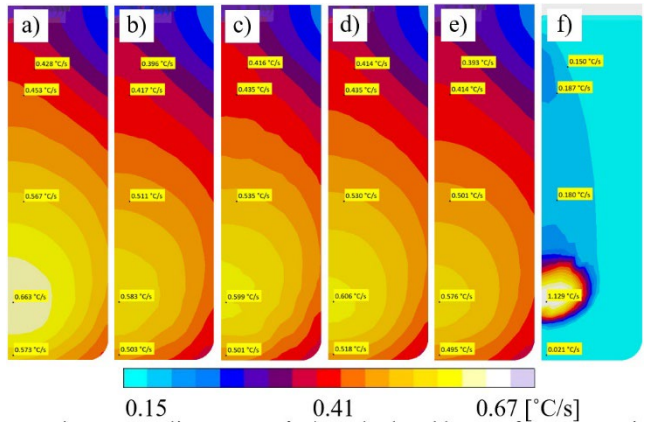


Fig. 14. Cooling rate R [˚C/s] calculated by T_S (f_s =100.0%) in the specimen made of: a) AlCu4Si6Fe1, b) AlCu4Si6Mn0.65, c) AlCu4Si6Fe1Mn0.65, d) AlCu4Si6Fe2, e) AlCu4Si6Mn2, f) AlCu10Si10Fe1

3.1.3.5. G and R calculated in the solidification range for solid fraction f_s=2, 25, 75 and 98%

The presented fields of gradient G and cooling rate R obtained from numerical simulation for the beginning (f_s=0.0%) and end of solidification (f_s=100%) indicate that the choice of their calculation temperature (TCT temperature in Magmasoft) is important and at each stage of solidification in the mushy zone different values of G and R may prevail. For three alloys (AlCu4Si6Fe1, AlCu4Si6Mn2 and AlCu10Si10Fe1), i.e. the most different in terms of the solid phase fraction curve (Fig. 3) and separated phases (Fig. 4), calculations were carried out for temperatures in the T_L-Ts range, for selected values of the solid fraction, e.g. f_s=2, 25, 75 and 98%. These f_s values correspond in each alloy to a slightly different value of their calculation temperature (TCT), which is given in detail in the figure captions (Fig. 15-20).

3.1.3.6. G and R for f_s=2, 25, 75 and 98% in the AlCu4Si6Fe1 alloy

Gradient G [˚C/mm] in the AlCu4Si6Fe1 alloy sample (Fig. 15) was calculated at Thermo Criteria Temperature (and % of solid fraction): a) 607.8 ˚C (2.0%), b) 595.0 ˚C (25%), c) 553.0 ˚C (75%), d) 529.0 ˚C (98%). At half the height of the sample, G reached values of 0.050, 0.149, 0.233, and 0.305 ˚C/mm for f_s=2, 25, 75, and 98%, respectively. In the upper part of the sample, G reached values of 0.133, 0.326, 0.350, and 0.356 ˚C/mm for f_s=2, 25, 75, and 98%, respectively. In the lower part (measurement area)of the sample, G reached values of 0.056, 0.105, 0.037, and 0.043 ˚C/mm. It is obvious that the G gradient takes on different values across the cross-section, in the upper and lower parts of the sample. In general, higher G values predominate in the upper and outer parts of the sample. As the f_s value increases, the G gradient values increase at mid-height and in the upper part of the sample. In the place of measurement (green rectangle area, Fig. 2), the situation is more complex.

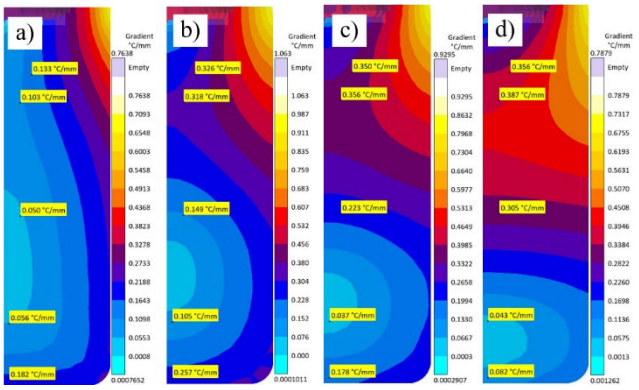


Fig. 15. Gradient G [˚C/mm] in the specimen made of AlCu4Si6Fe1 alloy and calculated by the Thermo Criteria Temperature (and % of solid fraction): a) 607.8 ˚C (2.0%), b) 595.0 ˚C (25%), c) 553.0 ˚C (75%), d) 529.0 ˚C (98%)

Analogously, the cooling rate R in the AlCu4Si6Fe1 alloy sample (Fig. 16) was calculated at Thermo Criteria Temperature (and % of solid fraction): a) 607.8 ˚C (2.0%), b) 595.0 ˚C (25%), c) 553.0 ˚C (75%), d) 529.0 ˚C (98%). At half the sample height, the cooling rate R reached values of 0.103, 0.205, 0.202, and 0.404 ˚C/s for f_s=2, 25, 75, and 98%, respectively. In the upper part of the AlCu4Si6Fe1 sample, the cooling rate R reached values of 0.146, 0.228, 0.212, and 0.289 ˚C/s for f_s=2, 25, 75, and 98%, respectively. Whereas in the lower part of the sample, in the measurement area, R reached values of 0.115, 0.180, 0.174, and 0.384 ˚C/s for f_s=2, 25, 75, and 98%, respectively. In the alloy under consideration, with the increase in the precipitated solid phase f_s, the cooling rate values increase, and therefore different thermal conditions prevail for the precipitation of phases, e.g., α-Al and β-$Al_9Fe_2Si_2$, at the beginning and end of the solidification process. Fig. 16 a-d clearly shows a tendency towards a change in the distribution of high and low values. At the beginning of solidification, f_s=2% (Fig. 16a), higher values were observed in the upper and outer parts of the sample, while at the end of solidification, at f_s=98%, the situation was reversed. In the lower part of the measurement, R assumes different values in the cylindrical axis of the sample and in the outer part, therefore, attention should be paid to the nature of these precipitates in individual areas.

In the AlCu4Si6Fe1 alloy, in the central part of the sample the β-$Al_9Fe_2Si_2$ phases that nucleated early at a temperature of about 595.0 ˚C (Fig. 4a, violet line, Table 2) precipitated at R of about 0.115 ˚C/s (Fig. 16a), whereas those that grew near the end of solidification (Fig. 4c, violet line, Table 2) precipitated at R of about 0.384 ˚C/s (Fig. 16d). Similar differences apply to the prevailing gradient G, i.e. around 595.0 ˚C it was about 0.105 ˚C/mm (Fig. 15a) and at the solidus the phases grew at G of about 0.043 ˚C/mm (Fig. 15d).

3.1.3.7. G and R for f_s=2, 25, 75 and 98% in the AlCu4Si6Mn2 alloy

Gradient G ˚C/mm in the AlCu4Si6Mn2 alloy sample (Fig. 17) was calculated at Thermo Criteria Temperature (and % of solid fraction): a) 636.0 ˚C (2.0%), b) 599.0 ˚C (25%), c) 552.0 ˚C (75%), d) 526.0 ˚C (98%). At half the height of the sample, G reached values of 0.179, 0.164, 0.205, and 0.252 ˚C/mm for f_s=2, 25, 75, and 98%, respectively. In the upper part of the sample, G reached values of 0.275, 0.323, 0.313, and 0.297 ˚C/mm for f_s=2, 25, 75, and 98%, respectively. In the lower part (measurement area, Fig. 2) of the sample, G reached values of 0.008, 0.089, 0.022, and 0.050 ˚C/mm. It is clear that the G gradient assumes different values across the cross-section, in the upper and lower sections of the sample. In general, higher G values predominate in the upper and outer sections of the sample. As the f_s value increases, the G gradient values generally increase at mid-height and in the upper section of the sample. In the measurement area, the situation is more complex, with higher values prevailing in the outer section than in the section located along the cylindrical axis of the sample.

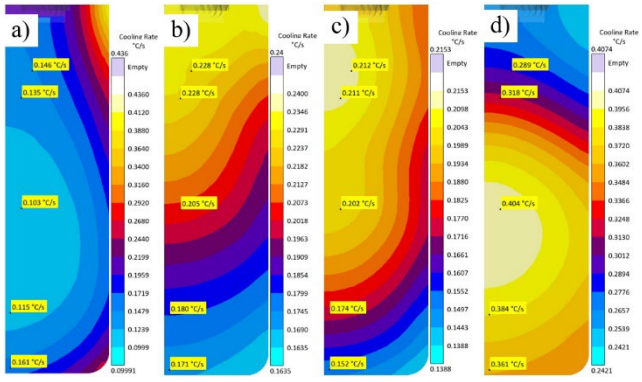


Fig. 16. Cooling rate R [˚C/s] in the specimen made of AlCu4Si6Fe1 alloy and calculated by the Thermo Criteria Temperature (and % of solid fraction): a) 607.8 ˚C (2.0%), b) 595.0 ˚C (25%), c) 553.0 ˚C (75%), d) 529.0 ˚C (98%)

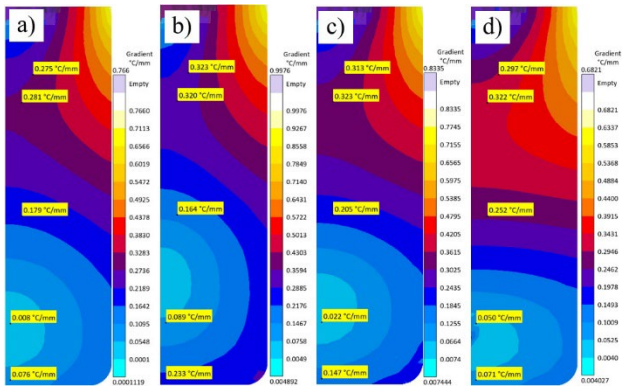


Fig. 17. Gradient G [˚C/mm] in the specimen made of AlCu4Si6Mn2 alloy and calculated by the Thermo Criteria Temperature (and % of solid fraction): a) 636.0 ˚C (2.0%), b) 599.0 ˚C (25%), c) 552.0 ˚C (75%), d) 526.0 ˚C (98%)

Analogously, the cooling rate R in the AlCu4Si6Mn2 alloy sample (Fig. 18) was calculated at Thermo Criteria Temperature (and % of solid fraction): a) 636.0 ˚C (2.0%), b) 599.0 ˚C (25%), c) 552.0 ˚C (75%), d) 526.0 ˚C (98%). At halfway up the sample, the cooling rate R reached values of 0.546, 0.208, 0.194, and 0.356 ˚C/s for f_s=2, 25, 75, and 98%, respectively. In the upper part, the cooling rate R reached values of 0.553, 0.226, 0.192, and 0.267 ˚C/s for f_s=2, 25, 75, and 98%, respectively. In the lower part of the sample (measurement area), the cooling rate R reached values of 0.539, 0.177, 0.179, and 0.329 ˚C/s for f_s=2, 25, 75, and 98%,

respectively. It is obvious that the cooling rate R assumes different values across the cross-section, in the upper and lower parts of the sample. In the alloy under consideration, with the increase in the precipitated solid phase f_s, the cooling rate values decrease from f_s=2% to 75% and then increase at f_s=98%, thus different thermal conditions prevail for the precipitation of phases, e.g., α-Al and $Al_{15}Si_2Mn_4$, at the beginning and end of the solidification process. According to Fig. 4b and 3a, it can be seen that at f_s=2% the alloy is at the stage of precipitation of the $Al_{15}Si_2Mn_4$ phase, which constitutes a small amount of the solid phase of the alloy (Fig. 3b), therefore the small amount of released heat of solidification L favors a high value of the cooling rate. The progressive, more intense solid phase growth (Fig. 3a) and larger amounts of heat released lower the R value. At the end of solidification, at f_s=98%, R increases again because most of the casting has already solidified and most of the heat has already been released and does not inhibit cooling, so R increases. Fig. 18 a-d clearly shows a trend toward a change in the distribution of high and low values. At the beginning of solidification, f_s=2% (Fig. 16a), higher R values prevailed in the upper and middle parts of the sample, while at the end of solidification, at f_s=98%, the situation was reversed. In the lower part of the measurement, R takes on different values in the cylindrical axis of the sample and in the outer part, therefore, attention should be paid to the nature of these precipitates in individual areas. In the AlCu4Si6Mn2 alloy, in the central part of the sample, the $Al_{15}Si_2Mn_4$ phases that nucleated early at the liquidus temperature T_L (Fig. 4b, yellow line, Tab. 2) precipitated at R of about 0.539 ˚C/s (Fig. 18a), whereas those that grew near the end of solidification (Fig. 4b, yellow line, Tab. 2) precipitated at R of about 0.329 ˚C/s (Fig. 18d). Similar differences apply to the prevailing gradient G, i.e. in the vicinity of the liquidus G was about 0.008 ˚C/mm (Fig. 17a) and at the solidus the phases grew at G of about 0.050 ˚C/mm (Fig. 17d).

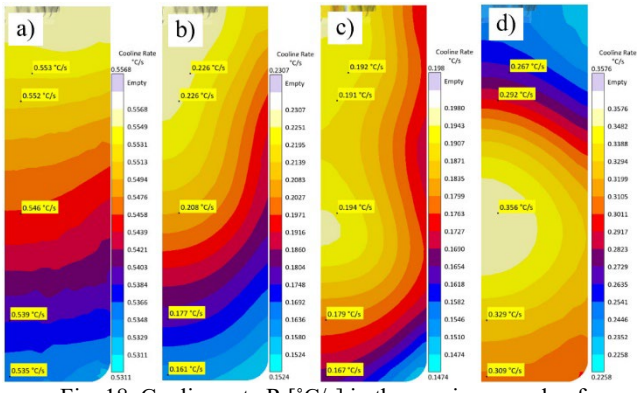


Fig. 18. Cooling rate R [˚C/s] in the specimen made of AlCu4Si6Mn2 alloy and calculated by the Thermo Criteria Temperature (and % of solid fraction): a) 636.0 ˚C (2.0%), b) 599.0 ˚C (25%), c) 552.0 ˚C (75%), d) 526.0 ˚C (98%)

3.1.3.8. G and R for f_s=2, 25, 75 and 98% in the AlCu10Si10Fe1 alloy

Gradient G [˚C/mm] (Fig. 19) in the AlCu10Si10Fe1 alloy sample was calculated at Thermo Criteria Temperature (and % of solid fraction): a) 575.0 ˚C (2.0%), b) 550.0 ˚C (25%), c) 521.9 ˚C (75%), d) 521.6 ˚C (98%). At half the height of the sample, G reached values of 0.155, 0.102, 0.166, and 0.262 ˚C/mm for f_s=2, 25, 75, and 98%, respectively. In the upper part of the sample, G reached values of 0.215, 0.230, 0.205, and 0.321 ˚C/mm for f_s=2, 25, 75, and 98%, respectively. In the lower part (place of measurement, Fig. 2) of the sample, G reached values of 0.021, 0.071, 0.065, and 0.165 ˚C/mm. The G gradient assumes different values across the cross-section, in the upper and lower parts of the sample. In general, higher G values prevail in the upper and outer parts of the sample, but for f_s=98%, the situation is more complicated. As the f_s value increases, the G gradient values generally increase. In the measured part, the situation is more complex, with higher values in the outer part for f_s=2, 25, and 75% and lower values for f_s=98% in the part located along the cylindrical axis of the sample.

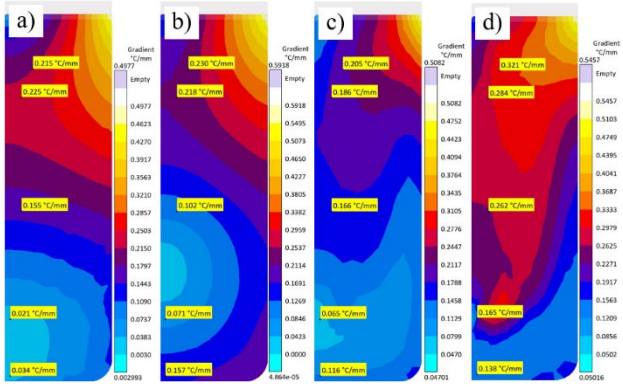


Fig. 19. Gradient G [˚C/mm] in the specimen made of AlCu10Si10Fe1 alloy and calculated by the Thermo Criteria Temperature (and % of solid fraction): a) 575.0 ˚C (2.0%), b) 550.0 ˚C (25%), c) 521.9 ˚C (75%), d) 521.6 ˚C (98%)

Analogously calculated cooling rate R (Fig. 20) in the AlCu10Si10Fe1 alloy sample was calculated at Thermo Criteria Temperature (and % of solid fraction): a) 575.0 ˚C (2.0%), b) 550.0 ˚C (25%), c) 521.9 ˚C (75%), d) 521.6 ˚C (98%). At halfway up the sample, the cooling rate R reached values of 0.474, 0.096, 0.101, and 0.161 ˚C/s for f_s=2, 25, 75, and 98%, respectively. In the upper part, the cooling rate R reached values of 0.465, 0.115, 0.074, and 0.131 ˚C/s for f_s=2, 25, 75, and 98%, respectively. In the lower part of the sample (place of measurement, Fig. 2), the cooling rate R reached values of 0.475, 0.081, 0.219, and 0.862 ˚C/s for f_s=2, 25, 75, and 98%, respectively. The cooling rate R assumes different values across the cross-section in the upper and lower parts of the sample. In the alloy under consideration, as the precipitated solid phase f_s increases from 2% to 75%, the R values generally decrease in the upper and middle parts, but continue to increase at f_s=98%. In the lower part of the sample (measurement area), the R values are lowest for f_s=25% and continue to increase to the highest value of 0.862 at f_s=98%. In the lower part, the situation is complex. Generally, R in this alloy adopts a complex and different distribution for f_s. For f_s=2%, the values are relatively uniform across the entire sample surface. For f_s=25%, higher values are found in the upper part, while for f_s=75% and 98%, the highest values are found in the lower part of the sample in the cylindrical axis, where they are extreme. The high R value at the beginning of solidification for f_s=2% is caused by the small amount of precipitated solid phase and heat, as shown in Fig. 3. At the end of

solidification, lower R values are caused by the intense precipitation of the solid phase (Fig. 3a). The highest R values observed for f_s=98% and the lower part result from the fact that this is the last region to solidify in the sample (Fig. 9f). Almost the entire sample has solidified, so there is no latent heat to inhibit cooling, and therefore R increases. The sample experiences different thermal conditions for the precipitation of phases, e.g., α-Al and $Al_{15}Si_2Mn_4$, at the beginning and end of the solidification process. In the AlCu10Si10Fe1 alloy, in the central part of the sample the β-$Al_9Fe_2Si_2$ phases that nucleated early at the liquidus temperature T_L (Fig. 4c, violet line, Table 2) precipitated at R of about 0.475 ˚C/s (Fig. 20a), whereas those that grew near the end of solidification (Fig. 4c, violet line, Table 2) precipitated at R of about 0.862 ˚C/s (Fig. 20d). Similar differences apply to the prevailing gradient G, i.e. in the vicinity of the liquidus G was about 0.021 ˚C/mm (Fig. 19a) and at the solidus the phases grew at G of about 0.165 ˚C/mm (Fig. 19d).

Comparison of the AlCu4Si6Fe1 alloy (Figs. 15-16) with the AlCu4Si6Mn2 (Figs. 17-18) and AlCu10Si10Fe1 alloy (Figs. 19-20), calculated for different solidification stages (solid fraction, temperature) determined for temperatures in the T_L-T_S range, showed differences in thermal conditions strongly determined by the solid fraction curve depending on the alloy composition. When analyzing the microstructures formed in the tested alloys and samples, one should remember about the variable course of the temperature gradient and cooling rate, because the size and shape of the precipitates (α-Al, β-$Al_9Fe_2Si_2$ α-$Al_{15}Si_2Mn_4$ crystals, Al-Si eutectics, etc.) may depend on the thermal conditions.

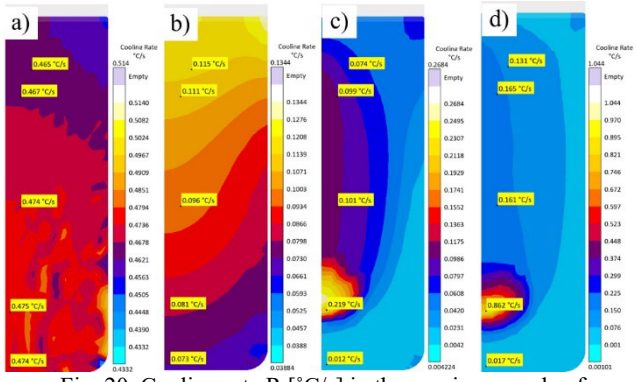


Fig. 20. Cooling rate R [˚C/s] in the specimen made of AlCu10Si10Fe1 alloy and calculated by the Thermo Criteria Temperature (and % of solid fraction): a) 575.0 ˚C (2.0%), b) 550.0 ˚C (25%), c) 521.9 ˚C (75%), d) 521.6 ˚C (98%)

3.2. Numerical prediction of eutectic spacing and secondary dendrite arm spacing SDAS

Currently, casting simulation software, in addition to flow (Navier-Stockes), thermal (Fourier-Kirckhoff), and stress models, also includes complex micromodels that enable modeling of the formation of casting microstructures, e.g., eutectic phase fraction [%], AlFeMnSi phase fraction, grain size, and SDAS spacing of secondary dendrite arms [µm]. However, micro modeling requires longer computational time, so SDAS can alternatively be predicted using formulas based on the thermal field.

3.2.1. Secondary dendrite arm spacing SDAS

Apart from the Microstructure Module, the secondary dendrite arm spacing (SDAS) $\lambda_2 = \lambda_{SDAS}$ (Fig. 21) in Magmasoft may be calculate based on:

$$\lambda_2 = c_1 \cdot (tS - tL)^{n_1} \quad (1)$$

where c_1 and n_1 are coefficients, by default c_1=11.03 and n_1=0.33 in the software used. The values obtained (Fig. 21a) for the AlCu4Si6Fe1 alloy are 76.418 µm in the middle of the sample and 77.104 in the bottom part where in the experiment measurement was conducted (Fig. 2b, green rectangle), and that is close to 79 µm from measurement (Tab. 1). For other alloys the differences in SDAS are larger, e.g. for AlCu4Si6Mn0.65 alloy, from simulation 79.784 µm and from measurement 100 µm was reached.

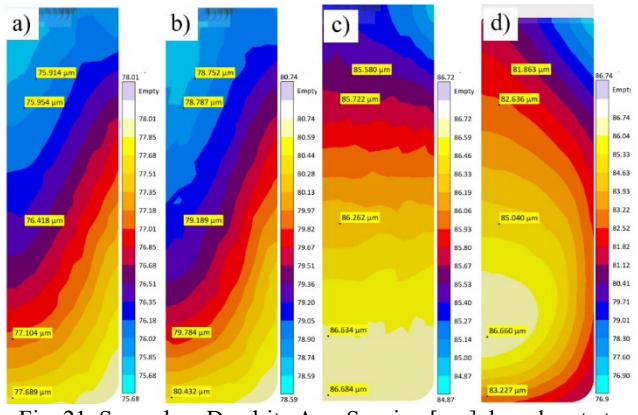


Fig. 21. Secondary Dendrite Arm Spacing [µm] based on t_S-t_L, c_1=11.03 and n_1=0.33 coefficients, in the specimen made of: a) AlCu4Si6Fe1, b) AlCu4Si6Mn0.65, c) AlCu4Si6Mn2 and d) AlCu10Si10Fe1 alloy

To ensure consistency between the simulations (Fig. 22) and the experimental data (Table 1), the n_1 coefficient values were left unchanged and the c_1 coefficient was optimized. The SDAS predictions suggested almost identical solidification conditions because a similar uniformity of values was obtained throughout the sample. For the tested alloys, the applied calculation formulas and optimized c_1 values are summarized in Table 3.

In metal alloys, the formation of dendritic structures is the subject of many studies, both computer modeling, e.g., models using the Phase Field Model (PFM) numerical method and experimental methods, e.g., using computed tomography and X-ray images. Among others, such investigations have shown that certain chemical composition and temperature disturbances may occur near the tip of the dendrite, leading to the formation of cellular structure, and later can form independent and in parallel growing arms, and finally can reach dendritical form. According to studies [57,58], the distance between secondary arms $\lambda_2 = \lambda_{SDAS}$ is determined by the thickening process that occurs during solidification. Furthermore, the studies [59-62] allowed the development of computational formulas for $\lambda_2 = \lambda_{SDAS}$ based on the solidification time:

$$\lambda_2 = c_1 \cdot (tS)^{n_1} \quad (2)$$

where n_1 = 0.33 or 0.48 and c_1 is materials coefficient [9,59-65].

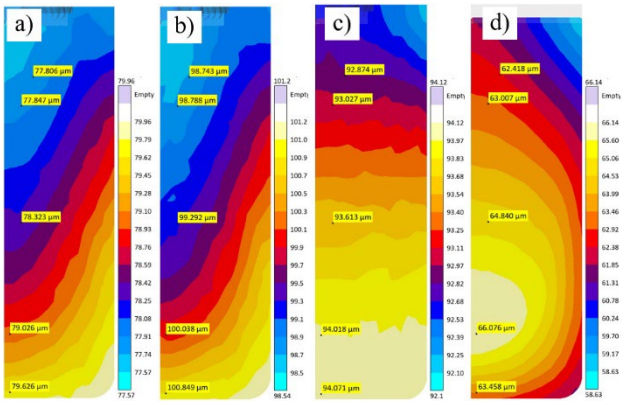


Fig. 22. Secondary Dendrite Arm Spacing [µm] based on t_S-t_L, n_1=0.33 and optimized c_1 coefficient, in the specimen made of: a) AlCu4Si6Fe1, b) AlCu4Si6Mn0.65, c) AlCu4Si6Mn2 and d) AlCu10Si10Fe1 alloy

Table 3.
Secondary Dendrite Arm Spacing SDAS calculated by different formulas and c_1 coefficients (from literature or optimized) for selected AlCuSi alloys specimens

SDAS [µm]		Alloys			
		AlCu4Si6Fe1	AlCu4Si6Mn0.65	AlCu4Si6Mn2	AlCu10Si10Fe1
Experimental		79.0	100.0	94.0	66.0
Simulated					
SDAS = $c_1 * (t_S-t_L)^{n_1}$	c_1=11.03	77.1	79.8	86.6	86.6
	c_1= …	(11.30)	(13.83)	(11.97)	(8.41)
		79.0	100.0	94.0	66.0
SDAS = $c_1 * (t_S)^{n_1}$	c_1=11.03	92.9	95.8	96.6	101.3
	c_1= …	(9.38)	(11.51)	(10.74)	(7.18)
		79.0	100.0	94.0	66.0
SDAS = $c_1 * (t_S-t_X)^{n_1}$	T_X= …	[553.0]	[552.0]	[552.0]	[521.7]
	c_1=11.03	48.6	50.6	51.6	49.7
	c_1= …	(17.93)	(21.79)	(20.09)	(14.65)
		79.0	100.0	94.0	66.0

(…) in the curly brackets the value of c_1 coefficient,
[…] in the square brackets, reached at the calculation time t_X, the temperature T_X.

Based on the solidification time t_S (formula (2)), with the optimized n_1 value (not the default n_1=0.33), the SDAS was calculated (Fig. 23) for the alloys a) AlCu4Si6Fe1, b) AlCu4Si6Mn0.65, c) AlCu4Si6Mn2 and d) AlCu10Si10Fe1. The n_1 optimization ensured the agreement between the simulation results and the experimental ones (Table 1) and provided the n_1 values for future SDAS predictions. The SDAS results suggest a very similar structure obtained in the lower, upper, inner and outer parts of the sample. For example, for the AlCu4Si6Fe1 alloy (Fig. 23 a), the SDAS in the lower part was 79.041 µm and in the upper part 77.654 µm.

A number of studies [9,57-65] have shown that when some arms melt and disappear at the end of solidification, despite the fact that secondary dendritic arms grow throughout the solidification process in hypoeutectic AlSi alloys, the SDAS distance to be established. During dendrite formation, phenomena of fragmentation, dendritic arm evolution, and coarsening occur [66-69], which can also be influenced by natural or forced convection [70]. Therefore, on this basis, it was decided to also calculate the SDAS based on the last 25% of the time in the T_L-T_S range. That is, instead of T_L-T_S, T_X = 552 ˚C was assumed for the AlCu4Si6Fe1, AlCu4Si6Mn0.65, and AlCu4Si6Mn2 alloys and 521.7 ˚C for the AlCu10Si10Fe1alloy. Then, we obtain the formula:

$$\lambda_2 = c_1 \cdot (tS - tX)^{n_1} \quad (3)$$

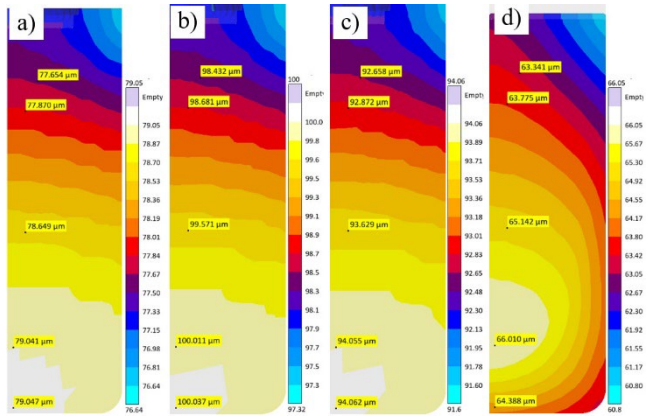


Fig. 23. Secondary Dendrite Arm Spacing [µm] based on t_S only, n_1=0.33 and optimized c_1 coefficient, in the specimen made of: a) AlCu4Si6Fe1, b) AlCu4Si6Mn0.65, c) AlCu4Si6Mn2 and d) AlCu10Si10Fe1 alloy

SDAS values (Fig. 24 a-c) show a similar distribution across the sample cross-section for AlCu4Si6Fe1, AlCu4Si6Mn0.65 and AlCu4Si6Mn2 alloys, higher values in the upper part and lower in the lower and middle part of the sample, e.g. 83.809 and 79.036 µm for AlCu4Si6Fe1 alloy. A completely opposite picture was obtained for AlCu10Si10Fe1alloy (Fig. 24 d) where the highest SDAS values are in the lower and middle part of the sample (66.008 µm) and the lowest in the upper part (46.614 µm), moreover, the difference between both values is more significant. It should be pointed out that the solid fraction curve for AlCu10Si10Fe1alloy (Fig. 3) as a result of the precipitation of individual phases (Fig. 4c), influences the cooling curve (Fig. 7) and most likely has an impact on the SDAS prediction.

Since the precipitation intensity (amount of solid phase) determines the arm thickness, degree of elongation, degree of dendrite growth, grain number, and probably also the spacing of

SDAS, based also on the results presented in Fig. 24, it was proposed that t_X depends on the degree of solid phase precipitation, and T_X was chosen widely from the T_L-T_S temperature range. An example SDAS prediction for the AlCu4Si6Fe1alloy alloy (Fig. 25) calculated using the Thermo Criteria Temperature (and % of solid fraction): a) 575.0 ˚C (2.0%), b) 550.0 ˚C (25%), c) 521.9 ˚C (75%), d) 521.6 ˚C (98%). It is clearly visible that as T_X changes, the distribution and values of SDAS change, which contributes to further research in the search for a new formula for SDAS simulation prediction.

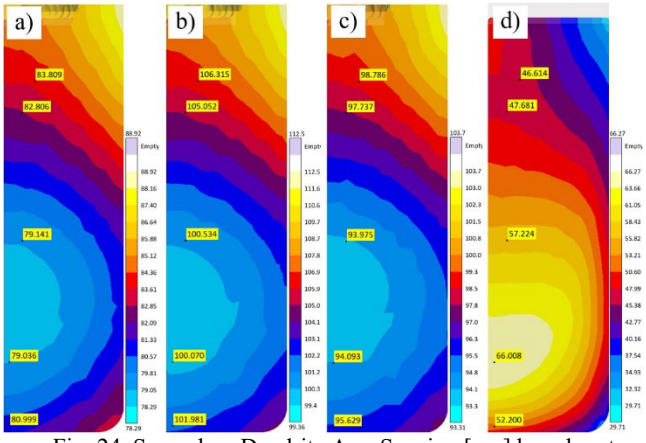


Fig. 24. Secondary Dendrite Arm Spacing [µm] based on t_S-t_X, n_1=0.33 and optimized c_1 coefficient, where t_X was calculated as last 25% of solid fraction curve (in T_L-T_S range), meaning solid fraction value of 75% (in point), in the specimen made of: a) AlCu4Si6Fe1, b) AlCu4Si6Mn0.65, c) AlCu4Si6Mn2 and d) AlCu10Si10Fe1alloy

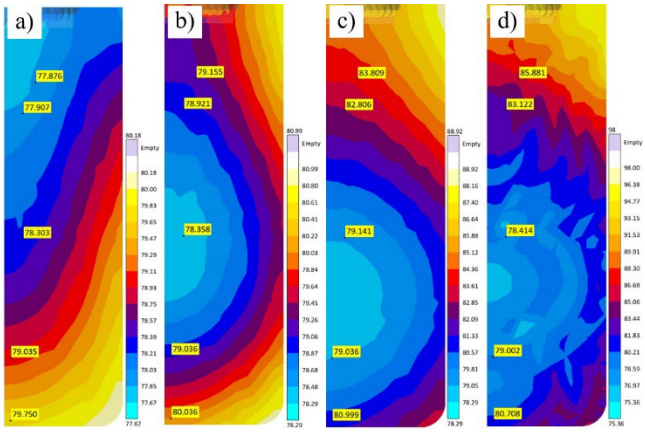


Fig. 25. Secondary Dendrite Arm Spacing [µm] based on t_S-t_X, n_1=0.33 and optimized c_1 coefficient, in the specimen made of AlCu4Si6Fe1alloy, where t_X (in T_L-T_S range) was calculated by chosen solid fraction (Feeding effectivity in MS): a) 2% (T_x=607.8 ˚C, c_1=11.36), b) 25% (T_x=595.0 ˚C, c_1=12.36), c) 75% (T_x=553.0 ˚C, c_1=17.94), d) 98% (T_x=529.0 ˚C, c_1=40.93)

3.2.2. Eutectic spacing EutSpa λ_E

Similarly to the spacing between dendrite arms, the characteristics of the eutectic structure in the alloy can be predicted. The classification of eutectics [71-73] is based on their growth mechanism and includes the divorced growth, where there is no exchange of solute between the two solid phases [71-73] and the cooperative growth where two (or more) phases grow together as a diffusion couple. The eutectic spacing λ_E may be determined [71-73] from simple formulation:

$$\lambda_E = c_2 \cdot (V)^{-0.5} \tag{4}$$

where V is solidification front velocity and c_2 is coefficient.

Since the solidification front velocity is not available in Magmasoft, the gradient and cooling rate were used to calculate it, and the c_2 coefficient was optimized. The λ_E values (Fig. 26), unlike SDAS, vary significantly across the sample cross-section, particularly in the AlCu10Si10Fe1 alloy (Fig. 26d). G and R were calculated at a specific temperature (or solid fraction) value indicated as TCT, which is assumed to be the solidus temperature in the case of eutectics. However, for eutectics, one could also identify a point at which the λ_E spacing value is determined, which may not necessarily be the end of solidification. However, based on Fig. 4, which gives the range of AlSi eutectics formation, e.g., from 560 to 525 ˚C for the AlCu4Si6Fe1 alloy, λ_E for R and G was calculated at: a) 550 ˚C (f_s=0.79), b) 540 ˚C (f_s=0.90), c) 530 ˚C (f_s=0.97), and d) 528 ˚C (f_s=0.98). The choice of the λ_E calculation temperature (Tables 4-5) is important for the upper part of the sample, where different values can be observed, while in the lower part, the λ_E values are identical because they were the goal of optimization. Both Figs. 26 and 27 indicate that λ_E in the lower measurement area (Fig. 2, green rectangle) takes different values, and the structures should be assessed carefully when studying the effects of solidification or convection.

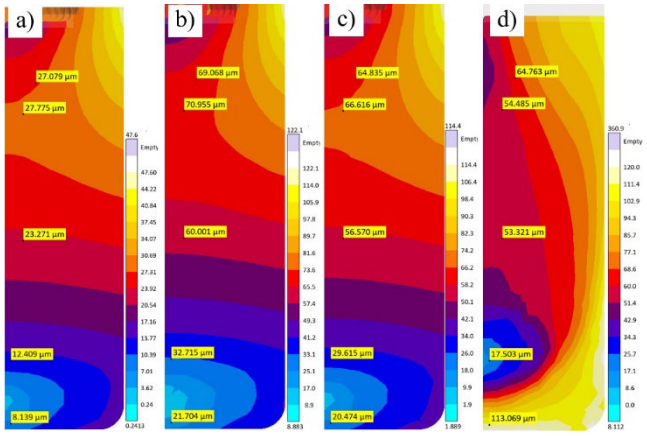


Fig. 26. Eutectic Spacing EutSpa [µm] of Al-Si eutectics based on V=f(R,G), n_2 = -0.5 and optimized c_2 coefficient, where R and G were calculated at solidus temperature (solid fraction 100%), in the specimens made of: a) AlCu4Si6Fe1, b) AlCu4Si6Mn0.65, c) AlCu4Si6Mn2 and d) AlCu10Si10Fe1 alloy

3.3. Effect of experimental procedure on thermal conditions

The influence of forced convection on the microstructure of alloys [30-35], including AlCuSi, was investigated in a device designed to ensure identical thermal conditions under variable convection conditions [51]. It was decided to estimate the variations in thermal conditions and indicate the possible influence on the microstructure formation conditions by assessing the solidification time as a representative parameter. For two selected alloys, AlCu4Si6Fe1 and AlCu10Si10Fe1, the influence of thermal conductivity of the graphite crucible and liquidus temperature, among others, was assessed. The results are summarized in Tables 6-13.

Table 4.
Eutectic Spacing EutSpa [µm] calculated by c_2 coefficient (optimized) for selected AlCuSi alloy specimens

EutSpa [µm] = c_2*(R/G)^n_2	Alloys			
	AlCu4Si6Fe1	AlCu4Si6Mn0.65	AlCu4Si6Mn2	AlCu10Si10Fe1
Experimental	12.4	32.7	29.6	17.5
Simulated	(27.43)	(70.93)	(68.36)	(41.69)
f_s=1.00,	12.4	32.7	29.6	17.6

(…) in the curly brackets the value of c_2 coefficient,

Table 5.
Eutectic Spacing EutSpa [µm] calculated by c_2 coefficients (optimized) for selected AlCu4Si6Fe1 alloy

EutSpa [µm] = c_2*(R/G)^n_2	Alloys			
	f_s=0.79 T= 550 ˚C	f_s=0.90 T= 540 ˚C	f_s=0.97 T= 530 ˚C	f_s=0.98 T= 528 ˚C
Experimental	12.4			
Simulated	(48.77)	(32.64)	(40.93)	(36.97)
	12.4	12.4	12.4	12.4

(…) in the curly brackets the value of c_2 coefficient,

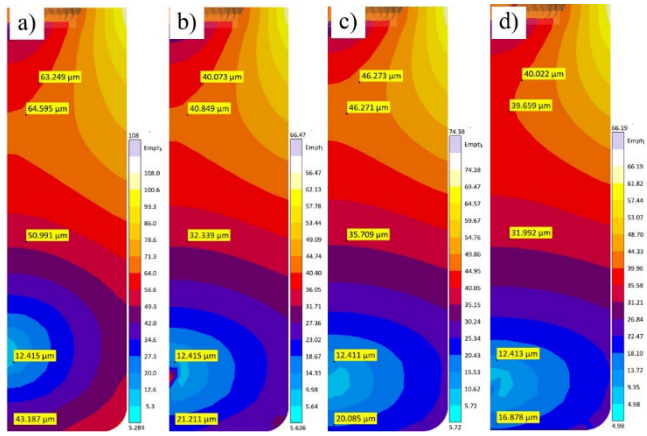


Fig. 27. Eutectic Spacing EutSpa [µm] of Al-Si eutectics based on V=f(R,G), n_2 = -0.5 and optimized c_2 coefficient, in the specimens made of AlCu4Si6Fe1, where R and G were calculated at: a) 550 ˚C (f_s=0.79), b) 540 ˚C (f_s=0.90), c) 530 ˚C (f_s=0.97) and d) 528 ˚C (f_s=0.98)

Due to the insulation around the crucible, and its heating effect during the experiments, the solidification time may be incorrectly estimated. Experiments earlier or later started may occur by various initial temperatures of Fiberfrax insulation. In the case of the AlCu4Si6Fe1 and AlCu10Si10Fe1 alloys (Table 6), increasing (earlier start of experiment) the initial temperature of Fiberfrax resulted in a delay in solidification by only 19 and 22 seconds.

Table 6.
Solidification time [s] in function of initial temperature of Fiberfrax insulation

Solidification time [s]	Initial temperature of insulation			
	20 ˚C	100 ˚C	200 ˚C	270 ˚C
AlCu4Si6Fe1	638	643	651	657
AlCu10Si10Fe1	828	834	845	850

The increase in the initial temperature of the alloy and graphite crucible from 800 to 850 ˚C, in the case of the AlCu4Si6Fe1 and AlCu10Si10Fe1 alloys (Table 7), resulted in an extension of the solidification time from 638 to 694 s and 828 to 903 s, respectively. The maximum and actual possible deviation of the initial temperature is exactly 5 ˚C, and hence a negligible extension of the solidification time by only 6 and 8 s.

Table 7.
Solidification time [s] in function of initial temperature of the crucible and the alloy

Solidification time [s]	Initial temperature of the crucible and the alloy				
	750 ˚C	795 ˚C	800 ˚C	805 ˚C	850 ˚C
AlCu4Si6Fe1	576	632	638	644	694
AlCu10Si10Fe1	751	821	828	836	903

During metallurgical furnace processing, sample size may change as slag and oxides are removed from the liquid alloy

surface. An incorrectly weighed portion of alloy, e.g., 262 g instead of the standard 201 g, can prolong solidification by 78 and 95 seconds for AlCu4Si6Fe1 and AlCu10Si10Fe1 alloys (Table 8). Because the samples are precisely cut, mass losses of approximately 5% are more realistic, which can result in negligible time reductions of only 10 and 19 seconds, respectively.

Table 8.
Solidification time [s] in function of the alloys assumed quantity and specimens assumed length

Solidification time [s]	The alloys quantity Specimens assumed mass 0.201 kg and length 67 mm						
	141 g 46.9 mm (-30%)	181 g 60.3 mm (-10%)	191 g 63.5 mm (-5%)	201 g 67.0 mm (0%)	211 g 70.3 mm (+5%)	221 g 73.7 mm (+10%)	262 g 87.1 mm (+30%)
AlCu4Si6Fe1	556	615	628	638	651	668	716
AlCu10Si10Fe1	710	793	809	828	846	862	923

Alloy components such as Al, Cu, Si, Fe, and Mn were precisely weighed and dosed into the furnace. Any changes in the liquidus temperature, e.g., 618.9 ˚C instead of 608.9 ˚C (Table 9), result in completely negligible changes in solidification time.

The cooling system protecting the coils from the hot insulation, crucible, and alloy is supplied with tap water at approximately 11˚C. Increasing the temperature of the copper chill to 91˚C due to an interruption in the water supply can extend solidification by 75 and 92 seconds for the AlCu4Si6Fe1 and AlCu10Si10Fe1 alloys, respectively (Table 10). With a constant water supply, the chill from starting temperature 11˚C can only reach a value of 21˚C, which can result in a completely negligible extension of the solidification time.

Table 9.
Solidification time [s] in function of the AlCu4Si6Fe1 alloys liquidus temperature

Solidification time [s]	Liquidus temperature of the alloy (assumed liquidus temperature 610 ˚C)				
	598.9 ˚C (-10 ˚C)	606.9 ˚C (-2 ˚C)	608.9 ˚C (0 ˚C)	610.9 ˚C (+2 ˚C)	618.9 ˚C (+10 ˚C)
AlCu4Si6Fe1	635.9	637.0	638.3	638.6	639.4

Table 10.
Solidification time [s] in function of the initial temperature of the cooling system

Solidification time [s]	The initial temperature of the cooling system			
	11 ˚C	21 ˚C	51 ˚C	91 ˚C
AlCu4Si6Fe1	638	639	669	713
AlCu10Si10Fe1	828	829	868	920

Crucibles used repeatedly for melting are cleaned (delicate lost of shape) and may also come from different suppliers, which can collectively affect their thermal properties. This effect was estimated based on the change in thermal conductivity of the graphite used in the crucibles. Increasing thermal conductivity (Table 11) from 64 W/mK to 70.4 W/mK resulted in reductions of only 5 and 7 seconds for both alloys tested.

Table 11.
Solidification time [s] in function of thermal conductivity of the graphite crucible

Solidification time [s]	Thermal conductivity of the graphite crucible				
	57.6 W/mK (-10 %)	60.8 W/mK (-5 %)	64 W/mK (0 %)	67.2 W/mK (+5 %)	70.4 W/mK (+10 %)
AlCu4Si6Fe1	643	640	638	636	633
AlCu10Si10Fe1	835	832	828	825	821

In contrast to previous studies on the effect of forced convection on microstructure [28,29], the current methodology aimed at slow bulk solidification, which was achieved by using a high initial crucible temperature. The effect of using the initial crucible temperature equal to the alloy temperature is presented in Table 12, which clearly shows that a temperature of 20 ˚C instead of 800 ˚C significantly shortened the solidification time of the samples, e.g. from 638 to 63 s for the AlCu4Si6Fe1 alloy. The correctness of the methodology has been confirmed.Tables 6-12 present the individual effects of various process factors on the solidification time of the tested samples. Assuming that all possible errors in the conducted solidification process could accumulate in a single experiment, leading to either an increase or decrease in solidification time, the cumulative effect was examined. Such a coincidence could lead (Table 13) to only a 19 s reduction in solidification time or a 29 s increase.

Table 12.
Solidification time [s] in function of initial temperature of the crucible

Solidification time [s]	Initial temperature of the crucible	
	20 ˚C	800 ˚C
AlCu4Si6Fe1	63	638
AlCu10Si10Fe1	73	828

Table 13.
Solidification time [s] in function of extreme values of parameters for AlCu4Si6Fe1 alloy

Extreme configuration of parameters variation	The variation of the studied parameter		
	in -	no variation	in +
Initial temperature of insulation	20 ˚C	20 ˚C	100˚C
Initial temperature of the alloy and the crucible	795 ˚C (-5 ˚C)	800 ˚C	805 ˚C (+5 ˚C)
The alloys amount variation from standard mass 0.201 kg	191 g, (-5 %)	201 g	211 g (+5 %)
The variation of the alloys liquidus temperature from 608.9 ˚C	606.9 ˚C (-2 ˚C)	610 ˚C	610.9 ˚C (+2 ˚C)
The variation of the initial temperature of the cooling system	11 ˚C	11 ˚C	21 ˚C
The variation of the graphite crucible's thermal conductivity	67.2 W/mK (+5 %)	64 W/mK	60.8 W/mK (-5%)
Solidification time [s]	619 (-19 s)	638	667 (+29 s)

(…) in the curly brackets the variation of the parameter in % or in unit.

Based on this, it can be assumed that the device design [47] and the experimental procedure used [30-35] to conduct slow solidification of many alloys, e.g. mentioned in the current paper (Table 1-2), ensure high reproducibility of the results and enable reliable comparison and assessment of the effect of convection on the structure.

4. Conclusions

Numerical simulation on solidification of AlCuSi alloys with Fe- and Mn-rich phases provided knowledge:

1. The simulation results confirmed the experimental data and the slow solidification of AlCuSi alloys, with a low gradient and cooling rate, by using a hot crucible and thermal insulation, effectively with cooling system pretending coils.
2. Cooling rate R and temperature gradient G numerically simulated in AlCuSi cylindrical samples presented various values depending on: the place in the sample (e.g. inside, or outside the cylinder), defined by alloys composition solid fraction curve, characteristic temperature or solid fraction of the R and G calculation.
3. In the studied alloys, the temperature gradient G calculated for liquidus temperature T_L has reached the values from 0.009 to 0.054 ˚C/mm in the bottom measurement place, whilst the values from 0.110 to 0.137 ˚C/mm for solidus temperature T_S. At half the sample height, G reached values from 0.034 to 0.156 ˚C/mm calculated for T_L, and from 0.294 to 0.408 ˚C/mm for T_S. The temperature of calculation determines the G values.
4. In the studied alloys, the cooling rate R calculated for liquidus temperature T_L has reached the values from 0.092 to 0.496˚C/s in the bottom measurement place, whilst the values from 0.576 to 1.129 ˚C/s for solidus temperature T_S. At half the sample height, R reached values from 0.082 to 0.520 ˚C/s calculated for T_L, and from 0.180 to 0.567 ˚C/s for T_S. The temperature of calculation determines the R values.
5. In the AlCu4Si6Fe1 alloy and in the sample center, the β-$Al_9Fe_2Si_2$ phases precipitated at G=0.050-0.103 ˚C/mm and R=0.103-0.135 ˚C/s near to liquidus temperature, whilst at G=0.043-0.387 ˚C/mm and R 0.318-0.404 ˚C/s near to solidus.
6. In the AlCu4Si6Mn2 alloy and in the sample center, the $Al_{15}Si_2Mn_4$ phases precipitated at G=0.008-0.281 ˚C/mm and R=0.539-0.552 ˚C/s near to liquidus temperature, whilst at G=0.050-0.322 ˚C/mm and R 0.292-0.356 ˚C/s near to solidus.
7. In the AlCu10Si10Fe1 alloy and in the sample center, the β-$Al_9Fe_2Si_2$ phases precipitated at G=0.021-0.225 ˚C/mm and R=0.467-0.475 ˚C/s near to liquidus temperature, whilst at G=0.165-0.284 ˚C/mm and R 0.151-0.862 ˚C/s near to solidus.
8. Because temperature gradient G and cooling rate R has reached values depending on solid fraction (in 0-1 range) or calculation temperature (in T_L-T_S range), the individual growing phases, e.g. $Al_9Fe_2Si_2$, α-Al, $Al_{15}Si_2Mn_4$ phase or AlSi eutectics, precipitated under different R and G.
9. In the prediction of secondary dendrite arm spacing and AlSi eutectic spacing new approach was tested and appropriate values of materials coefficient's have been established.
10. Negligible impact of errors in processing parameters set by experimental procedure was observed.

Acknowledgements

The research leading to these results has received partial funding from the People Programme (Marie Curie Actions) of the European Union's Seventh Framework Programme (FP7/2007–2013) under the REA grant agreement n° PCIG13-GA-2013-613906. More information on the funded projects is available at: www.iFlowFePhase.info. This research was partially founded by the Ministry of Science and Higher Education in Poland, allocated at Poznan University of Technology, grant number 0613/SBAD/4940.

References

[1] Shwe, W.H.A., Kay, T.L. & Waing, K.K.O. (2008). The effect of ageing treatment of aluminum alloys for fuselage structure-light aircraft. *International Journal of Materials and Metallurgical Engineering.* 2(10), 245-248.
[2] Miller, W.S., Zhuang, L., Bottema, J., Wittebrood, A.J., de Smet, P., Haszler A. & Vieregge A. (2000). Recent development in aluminum alloys for the automotive industry.

Journal of Materials Science and Engineering A. 280(1), 37–49. DOI: 10.1016/S0921-5093(99)00653-X.
[3] The Aluminum Association. (1998). *Aluminum alloy selection and applications*. Washington, D C.
[4] Cubberly, W.H. (1979). *Properties and selection: non-ferrous alloys and pure metals. Metals Handbook*. American Society for Metals.
[5] Smith, W.F. (1993). *Structure and properties of engineering alloys*. McGraw-Hill.
[6] Mondolfo, L.F. (1976). *Aluminium Alloys: Structure and Properties*. Butterworths & Co.: London, UK.
[7] Gao, N. (Ed.). (2018). *Aluminum alloys*. MDPI.
[8] Stefanescu, D. (1988). *The New Metals Hand Book.* ASM International.
[9] Ferreira, A.F., Castro, J.A. & Ferreira, L.O. (2017). Predicting secondary-dendrite arm spacing of the Al-4.5wt%Cu alloy during unidirectional solidification. *Materials Research*. 20(1), 68-75. DOI: 10.1590/1980-5373-MR-2015-0150.
[10] Barros, A.S., Magno, I.A., Souza, F.A., Mota, C.A., Moreira, A.L., Silva, M.A. & Rocha, O.L. (2015). Measurements of microhardness during transient horizontal directional solidification of Al-rich Al-Cu alloys: Effect of thermal parameters, primary dendrite arm spacing and Al_2Cu intermetallic phase. *Metals and Materials International.* 21(3), 429-439. DOI: 10.1007/s12540-015-4499-2.
[11] Lei, Q., Wang, J. & Misra, A. (2021). Mechanical behavior of Al–Al2Cu–Si and Al–Al2Cu eutectic alloys. *Crystals.* 11(2), 194, 1-9. https://doi.org/10.3390/cryst11020194.
[12] Flemings, M. (1991). Behavior of metal alloys in the semisolid state. *Metallurgical Transactions B*. 22B, 269-293. https://doi.org/10.1007/BF02651227.
[13] Kaldre, I., Milgravis, M., Bojarevics, A. & Beinerts, T. (2021). Electromagnetic processing during directional solidification of particle-strengthened aluminum alloys for additive manufacturing. *Materials Proceedings.* 3(1), 19, 1-4. https://doi.org/10.3390/IEC2M-09255.
[14] Wang, X.J., Zhao, Z.H., Zuo, Y.B., Zhu, Q.F., Qu, F. & Cui, J.Z. (2009). Effects of low frequency electromagnetic field on solidification of 7050 aluminium alloy during hot top casting. *Materials Science and Technology*. 25(10), 1207-1210. https://doi.org/10.1179/174328408X382172.
[15] Patarić A., Mihailović M., Marković M., Sokić M., Radovanović A. & Jordović B. (2021). Microstructure as an essential aspect of EN AW 7075 aluminum alloy quality influenced by electromagnetic field during continuous casting process. *Hemijska industrija*. 75(1), 31-37. DOI: 10.2298/HEMIND201214006P.
[16] Patarić A., Mihailovic M. & Gulisija Z. (2012). Quantitative metallographic assessment of the electromagnetic casting influence on the microstructure of 7075 Al alloy. *Journal of Materials Science.* 47, 793-796. DOI: 10.1007/s10853-011-5855-3.
[17] Zaïdat K., Mangelinck-Noël N. & Moreau R. (2007). Control of melt convection by a travelling magnetic field during the directional solidification of Al–Ni alloys. *Comptes Rendus Mecanique.* 335, 330-335. DOI:10.1016/j.crme.2007.05.010.
[18] Sree Manu, K.M., Barekar, N.S., Lazaro-Nebreda J., Patel, J.B. & Fan, Z. (2021). In-situ microstructural control of A6082 alloy to modify second phase particles by melt conditioned direct chill (MC-DC) casting process – A novel approach. *Journal of Materials Processing Technology.* 295, 117170, 1-10. https://doi.org/10.1016/j.jmatprotec.2021.117170.
[19] Zhang, Y., Patel, J.B., Lazaro-Nebreda, J. & Fan, Z. (2018). Improved defect control and mechanical property variation in high-pressure die casting of A380 alloy by high shear melt conditioning. *JOM*. 70, 2726-2730. https://doi.org/10.1007/s11837-018-3005-y.
[20] Wang, H., Davidson, C.J. & St. John, D.H. (2004). Semisolid microstructural evolution of AlSi7Mg during partial remelting. *Materials Science & Engineering: A.* 368(1-2), 159-167. https://doi.org/10.1016/j.msea.2003.10.305.
[21] Brollo, G.L., Proni, C.T.W. & Zoqui, E.J. (2018). Thixoforming of an Fe-Rich Al-Si-Cu alloy—thermodynamic characterization, microstructural evolution, and rheological behavior. *Metals*. 8(5), 332, 1-24. https://doi.org/10.3390/met8050332.
[22] Haga T. & Suziki, S. (2001). Casting of aluminum alloy ingots for thixoforming using a cooling slope. *Journal Materials Processing Technology*. 118 (1-2), 169-172. https://doi.org/10.1016/S0924-0136(01)00888-3.
[23] Eslami, M., Payandeh, M., Deflorian, F., Jarfors, A.E.W. & Zanella, C. (2018). Effect of segregation and surface condition on corrosion of Rheo-HPDC Al–Si alloys. *Metals*. 8(4), 209, 1-18. https://doi.org/10.3390/met8040209.
[24] Mohammed, M.N., Omar, M.Z., Al-Zubaidi, S., Alhawari, K.S. & Abdelgnei, M.A. (2018). Microstructure and mechanical properties of thixowelded AISI D2 tool steel. *Metals*. 8(5), 316, 1-16. https://doi.org/10.3390/met8050316.
[25] Eskin D.G. & Katgerman L. (2009). Solidification phenomena related to direct chill casting of aluminium alloys: fundamental studies and future challenges. *Materials Technology: Advanced Performance Materials.* 24(3), 152-156. DOI: 10.1179/106678509X12489478523537.
[26] Zhang, H., Nagaumi H. & Cui, J.Z. (2012). Effects of low frequency electromagnetic field of multi-physical fields during DC casting of 7XXX aluminum alloys. *Advanced Science Letters*. 13(1), 306-311. https://doi.org/10.1166/asl.2012.3762.
[27] Bojarevičs, A., Kaldre, I., Milgrāvis, M., Beinerts, T. (2017). Direct chill casting of aluminium alloys under electromagnetic interaction. In VIII International Scientific Colloquium "Modelling for Materials Processing", 21-22 September 2017 (pp. 259-262). Riga, Latvia. DOI: 10.22364/mmp2017.42.
[28] Mikolajczak, P. & Ratke, L. (2013). Effect of stirring induced by rotating magnetic field on β-Al5FeSi intermetallic phases during directional solidification in AlSi alloys. *International Journal of Cast Metals Research*. 26(6), 339-353. https://doi.org/10.1179/1743133613Y.0000000069.
[29] Mikolajczak, P. & Ratke, L. (2011). Intermetallic phases and microstructure in AlSi alloys influenced by fluid flow. *The Minerals, Metals & Materials Society. TMS*. 10, 9781118062173, 825-832. https://doi.org/10.1002/9781118062173.ch104.
[30] Mikolajczak, P. (2026). AlSiMg alloys microstructure determined by flow effect during slow solidification. *Archives*

of Foundry Engineering. 26(1), 52-67. DOI: 10.24425/afe.2026.157969.
[31] Mikolajczak, P. (2021). Effect of rotating magnetic field on microstructure in AlCuSi alloys. *Metals*. 11(11), 1804, 1-23. https://doi.org/10.3390/met11111804.
[32] Mikolajczak, P. (2023). Morphology and distribution of α-Al and Mn-rich phases in Al-Si-Mn alloys under an electromagnetic stirring. *Archives of Foundry Engineering*. 23(3), 74-87. DOI: 10.24425/afe.2023.146665.
[33] Mikolajczak, P. (2023). Flow effect on Si crystals and Mn-phases in hypereutectic and eutectic Al-Si-Mn alloys. *Archives of Foundry Engineering*. 23(4), 72-86. DOI: 10.24425/afe.2023.146681.
[34] Mikolajczak, P. (2023). Distribution and morphology of α-Al, Si and Fe-rich phases in Al–Si–Fe alloys under an electromagnetic field. *Materials*. 16(9), 3304, 1-31. https://doi.org/10.3390/ma16093304.
[35] Mikolajczak, P. (2017). Microstructural evolution in AlMgSi alloys during solidification under electromagnetic stirring. *Metals*. 7(3), 89, 1-16. https://doi.org/10.3390/met7030089.
[36] Mikolajczak, P. (2025). Assessment of thermal conditions by slow solidification in Al alloys and the facility. *Archives of Foundry Engineering*. 25(2), 5-20. DOI: 10.24425/afe.2025.153788.
[37] Lv, G., Bao, Y., Zhang, Y., He, Y., Ma, W. & Leu, Y. (2018). Effects of electromagnetic directional solidification conditions on the separation of primary silicon from Al-Si alloy with high Si content. *Materials Science in Semiconductor Processing*. 81, 139-148. https://doi.org/10.1016/j.mssp.2018.03.006.
[38] He, Y., Yang, X., Duan, L., Li, S., Chen, Z., Ma, W., Lv, G. & Xing, A. (2021). Silicon separation and purification process from hypereutectic aluminum-silicon for organosilicon use. *Materials Science in Semiconductor Processing*. 121(1), 105333, 1-11. https://doi.org/10.1016/j.mssp.2020.105333.
[39] Wenzhou, Y., Wenhui, M., Guoqiang, L., Haiyang, X., Li, S. & Dai, Y. (2014). Effect of electromagnetic stirring on the enrichment of primary silicon from Al-Si melt. *Journal of Crystal Growth.* 405, 23-28. http://dx.doi.org/10.1016/j.jcrysgro.2014.07.035.
[40] Jie, J.C., Zou, Q.C., Wang, H.W., Sun, J.L., Lu, Y.P., Wang, T.M. & Li, T.J. (2014). Separation and purification of Si from solidification of hypereutectic Al-Si melt under rotating magnetic field. *Journal of Crystal Growth*. 399, 43-48. http://dx.doi.org/10.1016/j.jcrysgro.2014.04.003.
[41] Zhu, K., Hu, J., Ma, W., Wei, K., Lv, T. & Dai, Y. (2019). Effect of solidification parameters and magnetic field on separation of primary silicon from hypereutectic Ti-85 wt.% Si melt. *Journal of Crystal Growth*. 522, 78-85. https://doi.org/10.1016/j.jcrysgro.2019.05.012.
[42] Yoshikawa, T. & Morita, K. (2005). Refining of Si by the solidification of Si-Al melt with electromagnetic force. *ISIJ International*. 45(7), 967-971. https://doi.org/10.2355/isijinternational.45.967.
[43] Ma, X., Lei, Y., Yoshikawa, T., Zhao, B. & Morita, K. (2015). Effect of solidification conditions on the silicon growth and refining using Si-Sn melt. *Journal of Crystal Growth*. 430, 98-102. http://dx.doi.org/10.1016/j.jcrysgro.2015.08.001.
[44] Huang, F., Zhao, L., Liu, L., Hu, Z., Chen, R. & Dong, Z. (2019). Separation and purification of Si from Sn-30Si alloy by electromagnetic semi-continuous directional solidification. *Materials Science in Semiconductor Processing*. 99, 54-61. https://doi.org/10.1016/j.mssp.2019.04.015.
[45] Xue, H., Lv, G., Ma, W., Chen, D. & Yu, J. (2015). Separation mechanism of primary silicon from hypereutectic Al-Si melts under alternating electromagnetic fields. *Metallurgical and Materials Transactions A.* 46, 2922-2932. DOI: 10.1007/s11661-015-2889-1.
[46] Jiang, W., Yu, W., Li, J., You, Z., Li, C. & Lv, X. (2018). Segregation and morphological evolution of Si phases during electromagnetic directional solidification of hypereutectic Al-Si alloys. *Materials*. 12(1), 10, 1-14. DOI:10.3390/ma12010010.
[47] Sun, Jl., Zou, Qc., Jie, Jc. & Li, T. (2016). Separation of primary Si and impurity boron removal from Al-30%Si-10%Sn melt under a traveling magnetic field. *China Foundry.* 13(4), 284-288. https://doi.org/10.1007/s41230-016-6036-4.
[48] Zou, Q., Han, N., Zhang, Z., Jie, J., Xu, F. & An, X. (2020). Enhancing segregation behaviour of impurity by electromagnetic stirring in the solidification process of Al-30Si alloy. *Metals*. 10(1), 155, 1-11. DOI:10.3390/met10010155.
[49] Ren Z. & Junze J. (1992). Formation of a separated eutectic in Al-Si eutectic alloy. *Journal of Materials Science*. 27, 4663-4666. https://doi.org/10.1007/BF01166003.
[50] Zou, Q., Tian, H., Zhang, Z., Sun, C., Jie, J., Han, N. & An, X. (2020). Controlling segregation behaviour of primary Si in hypereutectic Al-Si alloy by electromagnetic stirring. *Metals*. 10(9), 1129, 1-13. https://doi.org/10.3390/met10091129.
[51] Mikolajczak, P., Janiszewski, J. & Jackowski, J. (2019). Construction of the facility for aluminium alloys electromagnetic stirring during casting. In Gapiński B., Szostak M., Ivanov V. (Eds.), *Advances in manufacturing II. Vol. 4. Mechanical Engineering* (pp. 164-175). Cham, Switzerland, Springer. https://doi.org/10.1007/978-3-030-16943-5_15.
[52] Magmasoft 6.0.0.6 - MAGMA Gießereitechnologie GmbH. Kackertstr. 16-18. 52072 Aachen. Germany. www.magmasoft.de.
[53] Thermo-Calc 4.1—Software package from Thermo-Calc Software AB. Stockholm. Sweden. Retrieved June 10, 2023 from www.thermocalc.se.
[54] Gustafsson, G., Thorvaldsson, T. & Dunlop, G.L. (1986). The influence of Fe and Cr on the microstructure of cast Al-Si-Mg alloys. *Metallurgical and Materials Transactions A*. 17, 45-52. https://doi.org/10.1007/BF02644441.
[55] Prakash, S.P., Om, P. & Devendra, K. (2020). Structure and mechanical behavior of in situ developed Mg_2Si phase in magnesium and aluminum alloys – a review. The Royal Society of Chemistry. *RSC Advances*. 10(61), 37327-37345. http://dx.doi.org/10.1039/D0RA02744H.
[56] Yan, F. (2013). *Development of high strength Al-Mg2Si-Mg based alloy for high pressure diecasting process*. PhD Thesis, BCAST, Brunel University Uxbridge, UB8 3PH United Kingdom.

[57] Hunt, J.D. (2001). Pattern formation in solidification. *Science and Technology of Advanced Materials.* 2, 147-155. https://doi.org/10.1016/S1468-6996(01)00040-7.
[58] Hunt, J.D. & Lu, S.Z. (1996). Numerical modeling of cellular/dendritic array growth: Spacing and structure predictions. *Metallurgical and Materials Transactions A.* 27, 611-623. https://doi.org/10.1007/BF02648950.
[59] Stefanescu, D. (2009). *Science and Engineering of Casting and Solidification*. Boston, MA, USA: Springer. https://doi.org/10.1007/b135947.
[60] Kattamis, T.Z. & Flemings, M.C. (1965). Dendrite morphology. Microsegregation and homogenization of low alloy steel. *Transactions of the Metallurgical Society of AIME.* 233(5), 992-999.
[61] Rappaz, M. & Boettinger, W. (1999). On dendritic solidification of multicomponent alloys with unequal liquid diffusion coefficients. *Acta Materialia.* 47(11), 3205-3219. https://doi.org/10.1016/S1359-6454(99)00188-3.
[62] Bouchard, D. & Kirkaldy, J.S. (1997). Prediction of dendrite arm spacing in unsteady- and steady-state heat flow. *Metallurgical and Materials Transactions B*. 28B, 651-663. https://doi.org/10.1007/s11663-997-0039-x.
[63] Steinbach, S. & Ratke, L. (2007). The influence of fluid flow on the microstructure of directionally solidified AlSi-base alloys. *Metallurgical and Materials Transactions A*. 38, 1388-1394. https://doi.org/10.1007/s11661-007-9162-1.
[64] Mortensen, A. (1991). On the rate of dendrite arm coarsening. *Metallurgical and Materials Transactions A*. 22, 569-574. https://doi.org/10.1007/BF02656824.
[65] Voorhees, P.W. & Glicksman, M.E. (1984). Ostwald ripening during liquid phase sintering—Effect of volume fraction on coarsening kinetics. *Metallurgical and Materials Transactions A*. 15A, 1081–1089. https://doi.org/10.1007/BF02644701.
[66] Neumann-Heyme, H., Shevchenko, N., Lei, Z., Eckert, K., Keplinger, O., Grenzer, J., Beckermann, C. & Eckert, S. (2018). Coarsening evolution of dendritic sidearms: From synchrotron experiments to quantitative modeling. *Acta Materialia*. 146, 176-186, ISSN 1359-6454, https://doi.org/10.1016/j.actamat.2017.12.056.
[67] Cool, T. & Voorhees, P.W. (2017). The evolution of dendrites during coarsening: Fragmentation and morphology. *Acta Materialia*. 127, 359-367, https://doi.org/10.1016/j.actamat.2017.01.029.
[68] Ruvalcaba, D., Eskin, D. G., Mathiesen, R. H., Arnberg, L. & Katgerman, L. (2009). Influence of dendrite arrangement on coarsening during solidification of high-solute Al alloys. *International Journal of Cast Metals Research*. 22(1-4), 271-274. https://doi.org/10.1179/136404609X367957.
[69] Terzi, S., Salvo, L., Suery, M., Dahle, A.K. & Boller, E. (2010). Coarsening mechanisms in a dendritic Al–10% Cu alloy. *Acta Materialia.* 58(1), 20-30. https://doi.org/10.1016/j.actamat.2009.08.052.
[70] Kasperovich, G., Genau, A. & Ratke, L. (2011). Mushy zone coarsening in an AlCu30 alloy accelerated by a rotating magnetic field. *Metallurgical and Materials Transactions A.* 42, 1657-1666. https://doi.org/10.1007/s11661-010-0542-6.
[71] Kurz. W, Fisher D.J. *Fundamentals of Solidification*. Switzerland: Trans Tech Publications.
[72] Dantzig, J.A., Rappaz, M. (2009). *Solidification*. Lausanne, Switzerland: EPFL Press.
[73] Jackson, K.A., Hunt, J.D. (1966). Lamellar and rod eutectic growth. *Transactions of the Metallurgical Society of AIME.* 236, 1129-1142.